

AFRL-VA-WP-TR-2006-3173

**PROPER ORTHOGONAL
DECOMPOSITION (POD)/RESPONSE
SURFACE METHODOLOGY (RSM)
METHODOLOGY FOR LOW
REYNOLDS NUMBER
AERODYNAMICS ON MICRO
AERIAL VEHICLE (MAV)**



Danny Liu and Lei Tang

**ZONA Technology, Inc.
9489 E. Ironwood Square Drive, Suite 100
Scottsdale, AZ 85258**

JULY 2006

Final Report for 08 April 2005 – 07 January 2006

This is a Small Business Innovation Research (SBIR) Phase I Report

Approved for public release; distribution is unlimited.

STINFO COPY

**AIR VEHICLES DIRECTORATE
AIR FORCE RESEARCH LABORATORY
AIR FORCE MATERIEL COMMAND
WRIGHT-PATTERSON AIR FORCE BASE, OH 45433-7542**

NOTICE AND SIGNATURE PAGE

Using Government drawings, specifications, or other data included in this document for any purpose other than Government procurement does not in any way obligate the U.S. Government. The fact that the Government formulated or supplied the drawings, specifications, or other data does not license the holder or any other person or corporation; or convey any rights or permission to manufacture, use, or sell any patented invention that may relate to them.

This report was cleared for public release by the Air Force Research Laboratory Wright Site (AFRL/WS) Public Affairs Office and is available to the general public, including foreign nationals. Copies may be obtained from the Defense Technical Information Center (DTIC) (<http://www.dtic.mil>).

AFRL-VA-WP-TR-2006-3173 HAS BEEN REVIEWED AND IS APPROVED FOR PUBLICATION IN ACCORDANCE WITH ASSIGNED DISTRIBUTION STATEMENT.

*//Signature//

TRENTON WHITE
Aerospace Engineer
Aerodynamic Configuration Branch
Aeronautical Sciences Division

//Signature//

DENNY MROZINSKI
Chief
Aerodynamic Configuration Branch
Aeronautical Sciences Division

//Signature//

PETER ERBLAND
Senior Technical Advisor
Aeronautical Sciences Division

This report is published in the interest of scientific and technical information exchange, and its publication does not constitute the Government's approval or disapproval of its ideas or findings.

*Disseminated copies will show “//signature//” stamped or typed above the signature blocks.

REPORT DOCUMENTATION PAGE				<i>Form Approved</i> OMB No. 0704-0188	
<small>The public reporting burden for this collection of information is estimated to average 1 hour per response, including the time for reviewing instructions, searching existing data sources, gathering and maintaining the data needed, and completing and reviewing the collection of information. Send comments regarding this burden estimate or any other aspect of this collection of information, including suggestions for reducing this burden, to Department of Defense, Washington Headquarters Services, Directorate for Information Operations and Reports (0704-0188), 1215 Jefferson Davis Highway, Suite 1204, Arlington, VA 22202-4302. Respondents should be aware that notwithstanding any other provision of law, no person shall be subject to any penalty for failing to comply with a collection of information if it does not display a currently valid OMB control number. PLEASE DO NOT RETURN YOUR FORM TO THE ABOVE ADDRESS.</small>					
1. REPORT DATE (DD-MM-YY) July 2006		2. REPORT TYPE Final		3. DATES COVERED (From - To) 04/08/2005 – 01/07/2006	
4. TITLE AND SUBTITLE PROPER ORTHOGONAL DECOMPOSITION (POD)/RESPONSE SURFACE METHODOLOGY (RSM) METHODOLOGY FOR LOW REYNOLDS NUMBER AERODYNAMICS ON MICRO AERIAL VEHICLE (MAV)				5a. CONTRACT NUMBER FA8650-05-M-3548	
				5b. GRANT NUMBER	
				5c. PROGRAM ELEMENT NUMBER 0605502	
6. AUTHOR(S) Danny Liu and Lei Tang				5d. PROJECT NUMBER A08Z	
				5e. TASK NUMBER	
				5f. WORK UNIT NUMBER 0C	
7. PERFORMING ORGANIZATION NAME(S) AND ADDRESS(ES) ZONA Technology, Inc. 9489 E. Ironwood Square Drive, Suite 100 Scottsdale, AZ 85258				8. PERFORMING ORGANIZATION REPORT NUMBER	
9. SPONSORING/MONITORING AGENCY NAME(S) AND ADDRESS(ES) Air Vehicles Directorate Air Force Research Laboratory Air Force Materiel Command Wright-Patterson AFB, OH 45433-7542				10. SPONSORING/MONITORING AGENCY ACRONYM(S) AFRL-VA-WP	
				11. SPONSORING/MONITORING AGENCY REPORT NUMBER(S) AFRL-VA-WP-TR-2006-3173	
12. DISTRIBUTION/AVAILABILITY STATEMENT Approved for public release; distribution is unlimited.					
13. SUPPLEMENTARY NOTES This is a Small Business Innovation Research (SBIR) Phase I report. PAO Case Number: AFRL/WS 06-1817, 26 July 2006.					
14. ABSTRACT This report was developed under a SBIR contract. The phase I project results in two major accomplishments that will facilitate the follow-on MAV design/analysis procedures. These are: a new computational (CFD) approach in the treatment of the low Reynolds number (low-Re) aerodynamics for airfoils and a proper orthogonal decomposition (POD) technique that is essential in providing a rapid CFD solution retrieval/reconstruction procedure for evaluations of forces, and moments for 3D MAV wings. Our low-Re aerodynamic method is based on Wilcox's transition/turbulence model concept in conjunction with a simple computational procedure using CFL3D for RANS simulation. Our method is found to yield correct locations of transition point, separation bubble and transition lengths for several low-Re airfoils including SD7003, Eppler387, La203a, and L VNIO9A. Other turbulence models were also exploited in that Spalart-Allmaras model was found to be superior in yielding the closest solutions with test data. Quasi-3D RANS simulation was performed using our simple low-Re aerodynamic model to investigate the vortex stretching effect of the laminar separation bubble. Finally, a POD technique is applied to a University of Florida MAV wing planform to demonstrate its reduced-order modeling capability.					
15. SUBJECT TERMS SBIR report, micro aerial vehicle (MAV), low-Reynolds number (low Re) flow, proper orthogonal decomposition, reduced-order method, flow transition, turbulence model, quasi-3D RANS simulation, SD7003 airfoil					
16. SECURITY CLASSIFICATION OF:			17. LIMITATION OF ABSTRACT: SAR	18. NUMBER OF PAGES 52	19a. NAME OF RESPONSIBLE PERSON (Monitor) Trenton White 19b. TELEPHONE NUMBER (Include Area Code) N/A
a. REPORT Unclassified	b. ABSTRACT Unclassified	c. THIS PAGE Unclassified			

TABLE OF CONTENTS

Section	Page
1.0 Activity Summary	1
2.0 Problem Statement	3
3.0 A First Try Using Low-Reynolds-Number Version of $k-\omega$ Model	6
4.0 RANS Simulation of Low-Reynolds-Number Airfoil Aerodynamics	10
5.0 Quasi-3D RANS Simulation of Low-Reynolds-number SD7003 Airfoil Case	30
6.0 RANS Simulation of University of Florida 5 In. MAV Wing	32
7.0 POD Reconstruction of MAV Wing Solution	35
8.0 Phase II Work Plan	37
9.0 References	42

LIST OF FIGURES

1 – Eppler 387 Airfoil Lift/Drag Polar (taken from [6])	3
2 – Leading Edge Separation Bubble (taken from [2])	4
3 – Results Showing Importance of Predicting LSB at low Re (taken from [7])	5
4 – Computational Grid	8
5 – Velocity Contours and Streamlines around SD7003 Airfoil	9
6 – Predicted Cp Distributions on the Upper Surface of SD7003 Airfoil	11
7 – Convergence History	11
8 – Velocity Field and Streamlines	13
9 – Predicted Surface Cp Distribution on a Coarser Mesh	14
10 – Velocity Fields Adjacent to the Upper Surface of SD7003 Airfoil	15
11 – Distribution of Tangential Mach Numbers	15
12 – Surface Cp Distributions Predicted by RANS with Zero Production Terms	17
13 – Convergence History	18
14 – Surface Cp Distributions Predicted by RANS with Transition	19
15 – Reynolds-stress Distributions	20
16 – Velocity Contours and Streamlines	21
17 – Distribution of Tangential Mach Numbers	22
18 – Computational Grids Used for Eppler387 Airfoil Cases	23
19 – Surface Cp Distributions for Eppler387 Airfoil Case	24
20 – Lift Curve for Eppler387 Airfoil Case	24
21 – Computational Grid Used for LA203A Airfoil Case	25
22 – Surface Cp Distributions for La203a Airfoil Case	26
23 – Computational Grid Used For LNV109A Airfoil Case	26
24 – Surface Cp Distributions for LNV109A Airfoil Case	27
25 – Computational Grid Used for FX63-137 Airfoil Case	28
26 – Surface Cp Distributions for FX63-137 Airfoil Case	29
27 – Computational Grid	30
28 – Laminar Surface Cp Distributions on the Upper Surface of SD7003 Airfoil	31
29 – S-A RANS Surface Cp Distributions on the Upper Surface of SD7003 Airfoil	31
30 – UF MAV: Flexible Latex Rubber Wing	32
31 – Computational Grid Blocks Layout	32
32 – Flow Patterns around University of Florida 5 in. MAV Wing	34
33 – POD Reconstructions of Surface Cp Distribution	36
34 – MAV 6-DOF Implemented in the Simulink Environment	40

1.0 ACTIVITY SUMMARY

This is our Phase I final report covering the period from 04/08/05 to 01/07/06. During this Phase I period, the following research and development (R & D) activities have taken place:

1.1 Revision of Phase I Statement of Works

Based on the suggestions given by our technical monitors during the kick-off meeting, we have revised our Phase I statement of works. The major tasks of our Phase I contract will be revised to the following R&D:

- Improve the capability of the current Navier-Stokes solvers for prediction of low-Reynolds-number (low-Re) airfoil aerodynamics by adding the transition prediction capability to the Navier-Stokes solvers.
- Validate the improved Navier-Stokes solver with Air Force Research Laboratory's (AFRL) low-Re SD7003 airfoil case.

1.2 Investigation of Low-Re Version of Wilcox's $k-\omega$ Model

Based on our previous experience, we first implement and test low-Re version of Wilcox's $k-\omega$ model for prediction of laminar separation bubble. Some preliminary results are presented in Section 3.0.

1.3 Reynolds Averaged Navier Stokes (RANS) Simulation of Low-Re Airfoil Aerodynamics

After the above warm-up exercise, a systematic RANS study of low-Re SD7003 airfoil case has been performed in Section 4.0. According to Unsteady Reynolds Averaged Navier Stokes (URANS) results presented in [17], Menter's 2-layer Baseline Shear Layer (BSL) model [25] and a low-Re version of Jones-Launder's $k-\varepsilon$ model [12] give the most accurate prediction of Reynolds stress. So, we have implemented Menter's 2-layer BSL model and Jones-Launder's $k-\varepsilon$ model [26] in NASA Langley's CFL3D code and compare with the existing S-A model [27] and Abid's low-Re $k-\varepsilon$ model [13] in the code. A simple procedure is developed to locate the position of separation induced transition for RANS simulation of low-Re airfoil aerodynamics. The robustness of the approach is further validated with several other low-Re airfoil cases.

1.4 Quasi-3D RANS Simulation of Low-Re SD7003 Airfoil Case

Quasi-3D RANS simulation of the same low-Re airfoil case is performed with three planes and periodic boundary condition in the spanwise direction. The objective is to investigate the vortex stretching effect on the predicted laminar separation bubble. The results will be presented in Section 5.0.

1.5 RANS Simulation of University of Florida 5in. Micro Air Vehicle (MAV) Wing

The improved RANS simulation method developed above will be applied to University of Florida 5in. MAV wing. The computational grids provided by Prof. Wei Shyy are refined in the normal direction. The results will be presented in Section 6.0 together with the laminar solutions.

1.6 Proper Orthogonal Decomposition (POD) Reconstruction of MAV Wing Solution

After obtaining CFD solutions at the selected training points, the so-called Proper Orthogonal Decomposition (POD) technique is further used to explore the reduced-order modeling. The results will be presented in Section 7.0.

2.0 PROBLEM STATEMENT

Recent advances in mechanical and electrical system miniaturization have spawned a growing interest in development of MAV's. These vehicles can be used to perform the military missions like battlefield management and damage assessment, biological and chemical agent detection, aerial reconnaissance, covert imaging as well as the civilian missions like traffic control, communications and data relay, and urban intelligence gathering.

A MAV is an order of magnitude smaller than a conventional one. Accordingly the tip Re ranges from about 20,000 to 500,000. Available in the literatures, there are only several experimental investigations into the airfoil aerodynamics at such low Re [1-5]. Compared with our understanding of high Re aerodynamics, our knowledge of low Re flows is very limited although there has been a long history of natural flight studies (e.g., insects and small birds).

2.1 Aerodynamics at Low Re

According to the limited studies in [1-5], the airfoil aerodynamics at low Re is found quite different from our more familiar aerodynamics at high Re . Due to large viscous effect, the flow at low Re is usually dominated by the formation of the leading edge separation bubble and other separation phenomena, which degrade the airfoil performance. Figure 1 presents the drag polar of the Eppler 387 airfoil, a well-documented low Re airfoil section, from [6]. A spike in the airfoil drag (C_d) is found for the lift coefficients (C_l) between 0.5 and 1.0 because of the formation and evolution of a leading edge separation bubble on the upper surface of the airfoil. Therefore, the accurate prediction of airfoil performance at low Re requires capturing the leading edge separation bubble computationally.

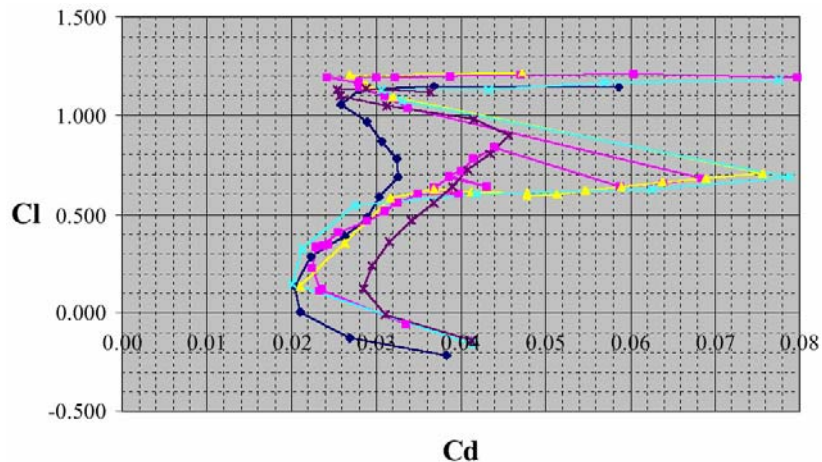


Figure 1 – Eppler 387 Airfoil Lift/Drag Polar (taken from [6])

The leading edge separation bubble is known as the result of a laminar boundary layer separation due to a large adverse pressure gradient after the point of minimum pressure. As shown in Figure 2, after the separation, the amplification of velocity disturbances causes the separated shear layer transition to turbulence. The resulting turbulent shear layer extracts more kinetic energy from the external flows and causes the flow reattached, forming a separation bubble.

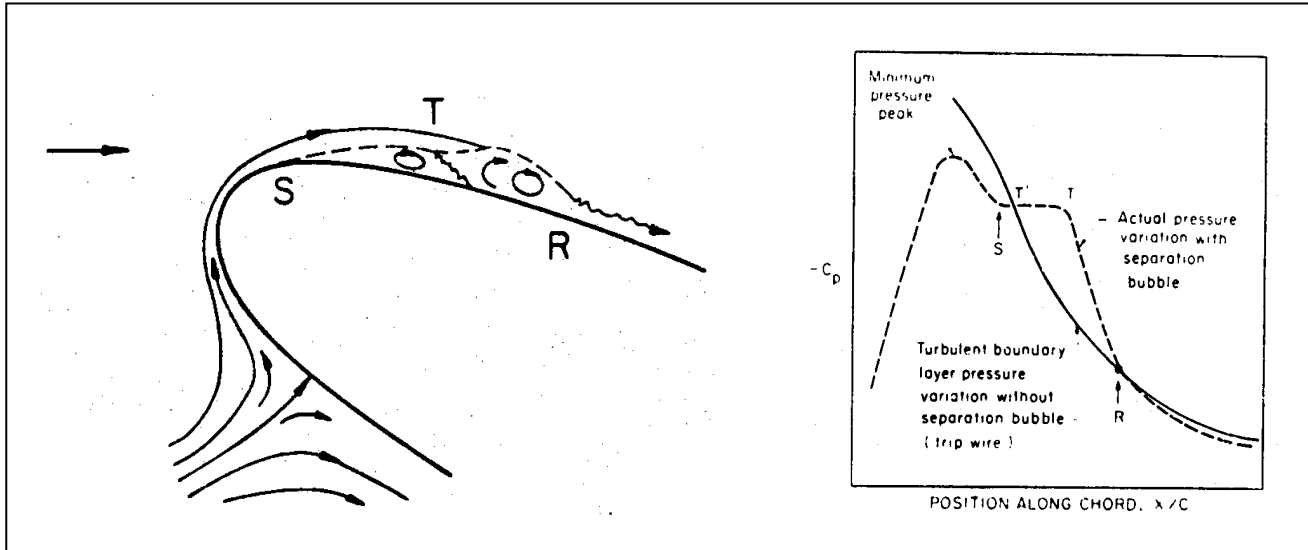


Figure 2 – Leading Edge Separation Bubble (taken from [2])

The transition of the separated shear layer from laminar to turbulent flow is the key in the formation and evolution of the leading edge separation bubble. It determines the size and shape of the bubble as well as the following turbulent boundary layer development. Many factors affect the transition position and width:

- Reynolds number
- Angle of attack
- Free stream disturbance
- Thickness of the boundary layer at separation
- Surface roughness.

The accurate prediction of this transition of the separated shear layer is really a challenging problem.

2.2 Prediction of Leading Edge Separation Bubble

From the above discussion, it is clear that the accurate prediction of airfoil performance at low Re requires capturing leading edge separation bubble numerically. As shown in Figure 3, which is taken from [7], without capturing the leading edge separation bubble, even the advanced Navier-Stokes approach is still unable to accurately predict the airfoil performance at low Re.

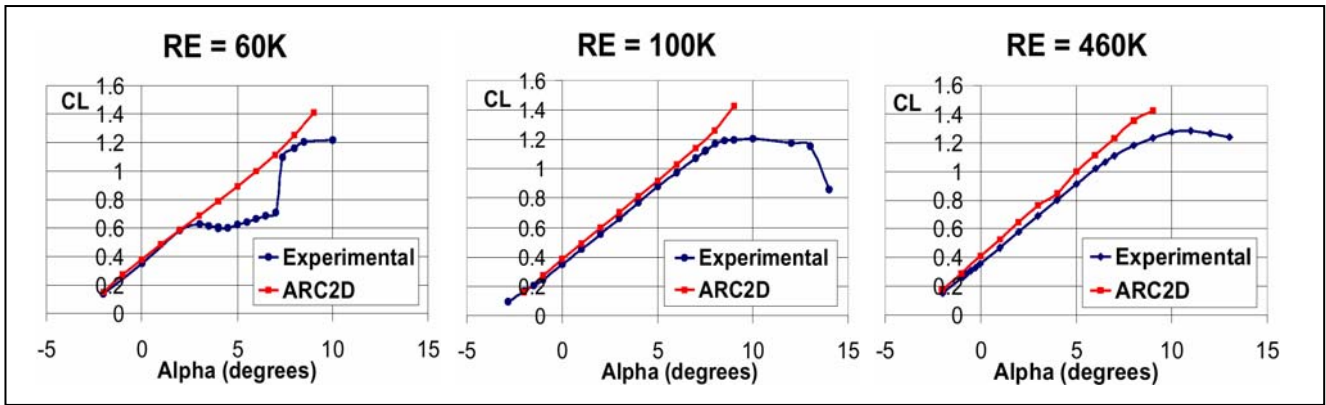


Figure 3 – Results Showing Importance of Predicting Leading Edge Separation Bubble at Low Re (taken from [7])

This situation prompts ZONA Technology to develop a computational algorithm suitable for prediction of the leading edge separation bubble. Since the transition of the separated shear layer from laminar to turbulent flow is the key in the formation and evolution of the leading edge separation bubble, the focus of our work is to develop the capability of predicting the transition from laminar to turbulent flow.

3.0 A FIRST TRY USING LOW-Re VERSION OF k - ω MODEL

Various computational approaches have been explored for prediction of low-Re aerodynamics, ranging from viscous/inviscid interactive methods (e.g., [8-11]) through RANS (e.g., [12-16]) and URANS (e.g., [17]) to large-eddy simulation (LES)/direct numerical simulation (DNS) (e.g., [17-18]) methods. Except RANS using low-Re version of turbulence models (e.g., [12-15]) and LES/DNS (e.g., [17-18]) in which the separation induced transition occurs naturally, all other approaches require an external mechanism to find the transition position. The method used in practice is still the semi-empirical e^N method [19-20] and its various approximations. In [8], for instance, Shum and Marsden used Van Ingen's shortcut e^N method for fast determination of the transition location. Drela and Giles came out a more sophisticated approximation, the so-called envelop method in [9] whereas Dini et al. adopted the table lookup approach in [10]. Stock and Haase, Yuan et al. further combined RANS and URANS with the e^N method in [16] and [17] respectively. The importance of sufficient grid resolution inside boundary layer has been emphasized in [16] for the accuracy of stability analysis based on the Navier-Stokes laminar solutions. On the other hand, although no need for an external transition mechanism, LES/DNS approach is computationally too intensive for engineering applications and the robustness of using a low-Re version of turbulence model for transition prediction is questionable. Whereas Wilcox presented some promising results for flat plate case in [14], the same low-Re version of Wilcox's k - ω model is found to predict the transition location too earlier in [15]. Furthermore, the transitional result given by a low-Re version of turbulence model is also found initial condition dependent [13].

In this section, as a warm-up exercise, we will first test the low-Re version of Wilcox's k - ω model [14] for the low-Re SD7003 airfoil case presented in [21]. Then in Section 4.0, we will further develop a simple method to locate the position of separation induced transition for RANS simulation of low-Re airfoil aerodynamics.

Transition Specific Wilcox's k - ω Turbulence Model

According to [14], the low Re version of Wilcox's k - ω turbulence model can be written as

$$\begin{cases} \frac{\partial}{\partial t}(\rho k) + \frac{\partial}{\partial x_j}(\rho u_j k) = \tau_{ij} \frac{\partial u_i}{\partial x_j} - \beta^* \rho \omega k + \frac{\partial}{\partial x_j} [(\mu + \sigma^* \mu_T) \frac{\partial k}{\partial x_j}] \\ \frac{\partial}{\partial t}(\rho \omega) + \frac{\partial}{\partial x_j}(\rho u_j \omega) = \alpha \frac{\omega}{k} \tau_{ij} \frac{\partial u_i}{\partial x_j} - \beta \rho \omega^2 + \frac{\partial}{\partial x_j} [(\mu + \sigma \mu_T) \frac{\partial \omega}{\partial x_j}] \end{cases} \quad (1)$$

with

$$\tau_{ij} = 2\mu_T \left(S_{ij} - \frac{1}{3} \frac{\partial u_k}{\partial x_k} \delta_{ij} \right) - \frac{2}{3} \rho k \delta_{ij} \quad (2)$$

$$\mu_T = \alpha^* \rho k / \omega \quad (3)$$

$$S_{ij} = \frac{1}{2} \left(\frac{\partial u_i}{\partial x_j} + \frac{\partial u_j}{\partial x_i} \right) \quad (4)$$

where t is time, x_j is spatial coordinate, ρ is density, u_j is velocity component, k is the turbulent kinetic energy, ω is specific dissipation rate, τ_{ij} is Reynolds stress tensor, μ is molecular viscosity, and μ_T is eddy viscosity.

In the form, the only difference of the low Re version of (1-4) from the original Wilcox's k - ω turbulence model is that there is a coefficient of α^* in front of $\rho k / \omega$ in (3) to introduce some low Re effect with α^* defined as

$$\alpha^* = \frac{\alpha_0 + Re_T / R_k}{1 + Re_T / R_k} \quad (5)$$

Other modifications are all included in the closure coefficients of α and β^* :

$$\alpha = \frac{5}{9} \frac{\alpha_0 + Re_T / R_\omega}{1 + Re_T / R_\omega} (\alpha^*)^{-1} \quad (6)$$

$$\beta^* = \frac{9}{100} \frac{5/18 + (Re_T / R_\beta)^4}{1 + (Re_T / R_\beta)^4}$$

while the other three closure coefficients of β , σ , σ^* are the same as those in the original model: $\beta = 3/40$ and $\sigma^* = \sigma = 1/2$. Here $\alpha_0^* = \beta/3$, $\alpha_0 = 1/10$, $R_\beta = 8$, $R_k = 6$, $R_\omega = 2.7$, and

$$Re_T = \frac{\rho k}{\omega \mu}.$$

With (3), the ω -equation in (1) can be rewritten as

$$\frac{\partial}{\partial t} (\rho \omega) + \frac{\partial}{\partial x_j} (\rho u_j \omega) = \alpha \rho [2\alpha^* (S_{ij} - \frac{1}{3} \frac{\partial u_k}{\partial x_k} \delta_{ij}) - \frac{2}{3} \omega \delta_{ij}] \frac{\partial u_i}{\partial x_j} - \beta \rho \omega^2 + \frac{\partial}{\partial x_j} [(\mu + \sigma \mu_T) \frac{\partial \omega}{\partial x_j}] \quad (7)$$

which is uncoupled from the k -equation in (1). Therefore, the k - ω model has a nontrivial laminar solution for ω , and we can start a computation in a laminar region with $k=0$ in the boundary layer and a small freestream value of k . Initially the production terms, the first two terms at the right hand side of both k - and ω -equations, are smaller than the dissipation term, the last term at the right hand side of both equations. Neither k nor ω is amplified and the flow remains laminar. After a point where the critical Re is achieved, the production terms start to exceed the dissipation term in the k -equation, and the turbulent energy is amplified. At some point in this process, the eddy viscosity grows rapidly and this corresponds to the transition point. After the production terms in the ω -equation further catches the dissipation term, ω is amplified and continues growing until a balance between production and dissipation is achieved in the k -equation. Then the transition from laminar to turbulent flow is completed [14].

Results and Discussion

The low-Re SD7003 airfoil case in [21] is selected for a systematic RANS study because a stable long separation bubble is found over the upper surface of the airfoil in the tests. The AFRL water tunnel test conditions are adopted as the flow conditions for computations. According to [21], the freestream Re based on the airfoil chord length is 60,000 and the angle of attack is 4° . The freestream Mach number and turbulence level are chosen as 0.0005 and 0.08 percent respectively. We also modify γ and Pr to fit the water property.

The SD7003 airfoil profile given by AFRL is shown in Figure 4. There are 280 points on the surface. We have added another 72 points to extend the grid to 5 chords in the wake region. A hyperbolic grid generator is used to generate the computational grid around the airfoil. There are 91 points in the normal direction with the first grid spacing of 10^{-5} chords to resolve the viscous layer.

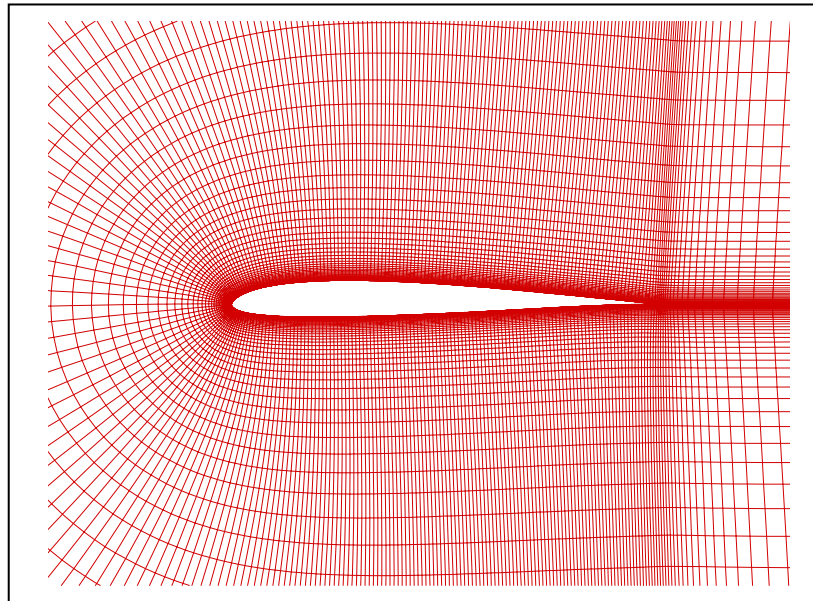


Figure 4 – Computational Grid

The CFD code used in this study is CFL3D v6 [22-23], which is developed and supported by NASA Langley. This is a three-dimensional thin-layer RANS solver, using an implicit, approximately factored, finite volume, upwind and multigrid algorithm. It employs formally third-order upwind-biased spatial differencing for the inviscid terms with flux limiting in the presence of shocks. Both flux-difference and flux-vector splitting methods are available in the code. The flux-difference splitting method of Roe is employed in the present computations for accurate viscous computations. On the other hand, the viscous terms are discretized with second-order central differencing. Since CFL3D is a compressible CFD code, Weiss-Smith low-Mach-number preconditioning technique [24] is used in the code to improve the convergence performance for incompressible flow simulation.

Figure 5 presents the predicted velocity contours and streamlines with comparison to the AFRL test data. It is found that our laminar result is very close to the test data except that the laminar

result gives two shorter separation bubbles instead of a single long separation bubble found in test. On the other hand, the use of the original Wilcox's $k-\omega$ turbulence model gives the flow without separation bubble. However, the use of the low-Re version of Wilcox's $k-\omega$ turbulence model improves the prediction of the flow pattern given by the laminar approach. Same as the test data, only one separation bubble is predicted.

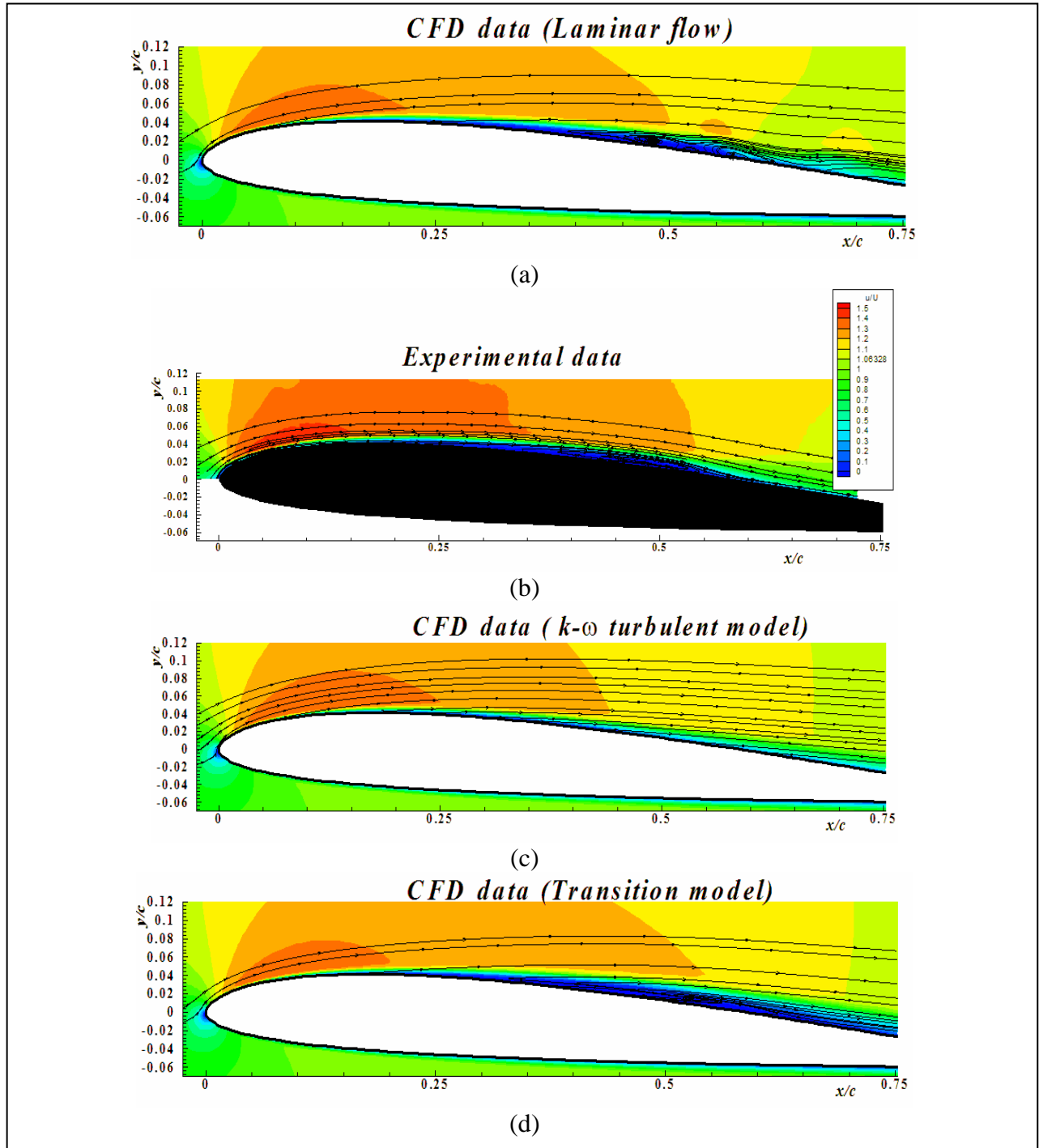


Figure 5 – Velocity Contours and Streamlines around SD7003 Airfoil

4.0 RANS SIMULATION OF LOW-RE AIRFOIL AERODYNAMICS

Although the above results using the low-Re version of Wilcox's $k-\omega$ model are promising, as mentioned earlier, the robustness of using a low-Re version of turbulence model for transition prediction is questionable. In this section, we will develop a simple method for RANS simulation to determine the position of separation induced transition from the obtained baseline laminar solution, similar to LES/DNS approaches.

Again, the low-Re SD7003 airfoil case in [21] is selected for a systematic RANS study. Instead of using AFRL's water tunnel conditions, however, the Technische Universitat Braunschweig (TU-BS) wind tunnel test conditions are adopted here as the flow conditions for computations. According to the standard atmosphere property, we estimate the Mach number to be 0.013. The computational grid used above is refined in the normal direction with 151 points instead of 91 points and the first grid spacing from the surface is 10^{-6} of the chord length. The outer boundaries of the grid are further extended to 20 chords in all directions.

4.1 Laminar Solution of Low-Re SD7003 Airfoil Case

A laminar computation is performed first. The predicted surface C_p distributions over the upper surface of the airfoil after 5,000, 10,000, 15,000, 20,000, 25,000, 30,000, and 35,000 iterations are presented in Figure 6. It is found that after 10,000 iterations, the obtained surface pressure coefficient (C_p) distribution is still like the one without the bubble perturbation. By that time, as shown in the convergence history presented in Figure 7, the numerical residual has already dropped by three orders of magnitude. So, most people may stop the computation there. They thought that a fully converged solution is obtained and without any external transition mechanism, the existing CFD approach is not able to capture the laminar separation bubble. However, if one is not fooled by the misleading convergence history and keeps running the computation, after 15,000 iterations, as shown in Figure 6, a surface C_p distribution with the bubble perturbation starts to be captured in the computations, with a C_p plateau between the separation and transition. After 25,000 iterations, the predicted surface C_p distribution becomes quite stable. This is different from Pauley et al.'s finding in [28], where a two-dimensional laminar separation solution is found quite unstable.

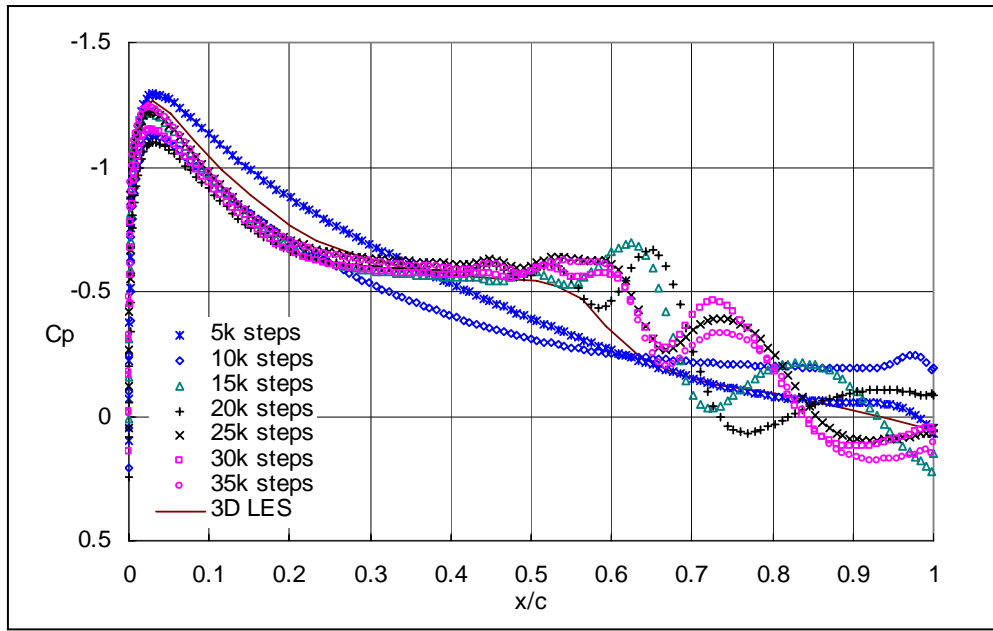


Figure 6 – Predicted Surface Cp Distributions on the Upper Surface of SD7003 Airfoil

Also shown in Figure 6 is the 3D LES result from [17]. It is found that our converged laminar solution agrees with the LES solution relatively well up to the transition point. After the transition point, there is a much larger discrepancy between the two solutions. Most notably, different from the LES result, our converged laminar solution has several artificial humps in the surface Cp distribution after the transition point. Looking from DNS point of view, this indicates that our employed numerical method and mesh are able to resolve the simulated laminar flow quite well but still unable to resolve the turbulent flow yet. A proper turbulence model is required for simulation of the flow after the transition point.

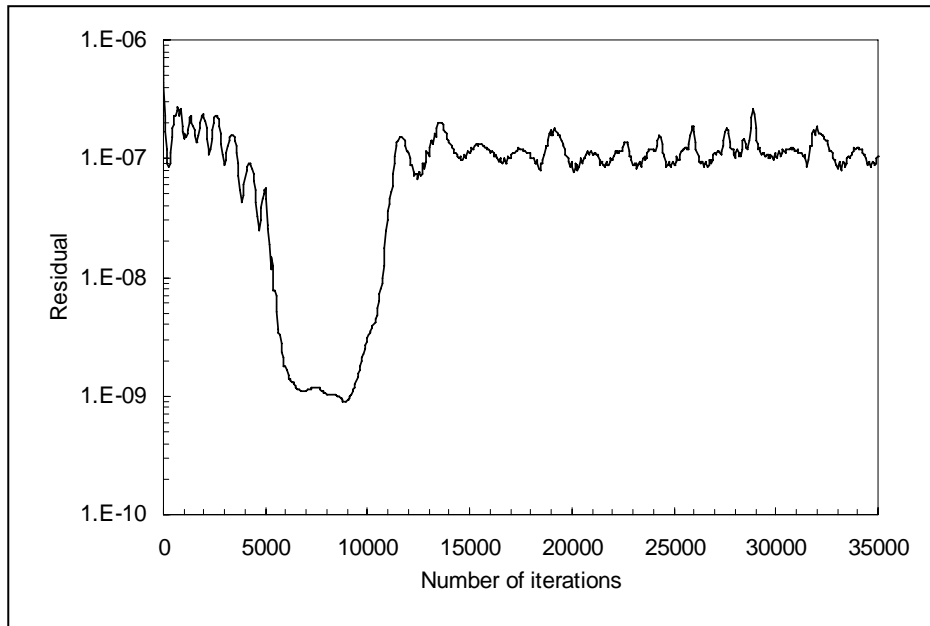


Figure 7 – Convergence History

It is noteworthy that after 9,000 iterations, as shown in Figure 7, the numerical residual quickly jumps by two orders of magnitude and oscillates around that level. As will be shown later, this is solely because we do not turn on a turbulence model from the transition point in the computation. Based on the surface C_p distribution shown in Figure 6 and the velocity fields shown in the following Figure 8, the big jump of numerical residual after 9,000 iterations indicates the transition of the numerical solution from one without the bubble perturbation to the one with the bubble perturbation.

Figure 8 further presents the predicted velocity fields, including some streamlines, after 5,000, 10,000, 15,000, 20,000, 25,000, 30,000, and 35,000 iterations and compares with AFRL test data in [21]. It is found that the flowfield solution obtained after 5,000 iterations has no separation at all. By 10,000 iterations, the trailing-edge separation is captured and by 15,000 iterations, the laminar separation bubble further starts to be captured. After 25,000 iterations, the predicted flow patterns are quite stable. All these observations are consistent with the surface C_p surface distributions shown in Figure 6. Compared with AFRL test data, the converged laminar solution of the separation bubble is much longer and thicker because there are three vortical structures inside the separation bubble instead of one found in the test. This also explains those artificial humps found in the converged surface C_p distribution shown in Figure 6. Apparently, the latter two vortical structures are due to the lack of transition to turbulence in the computation and they are not physical.

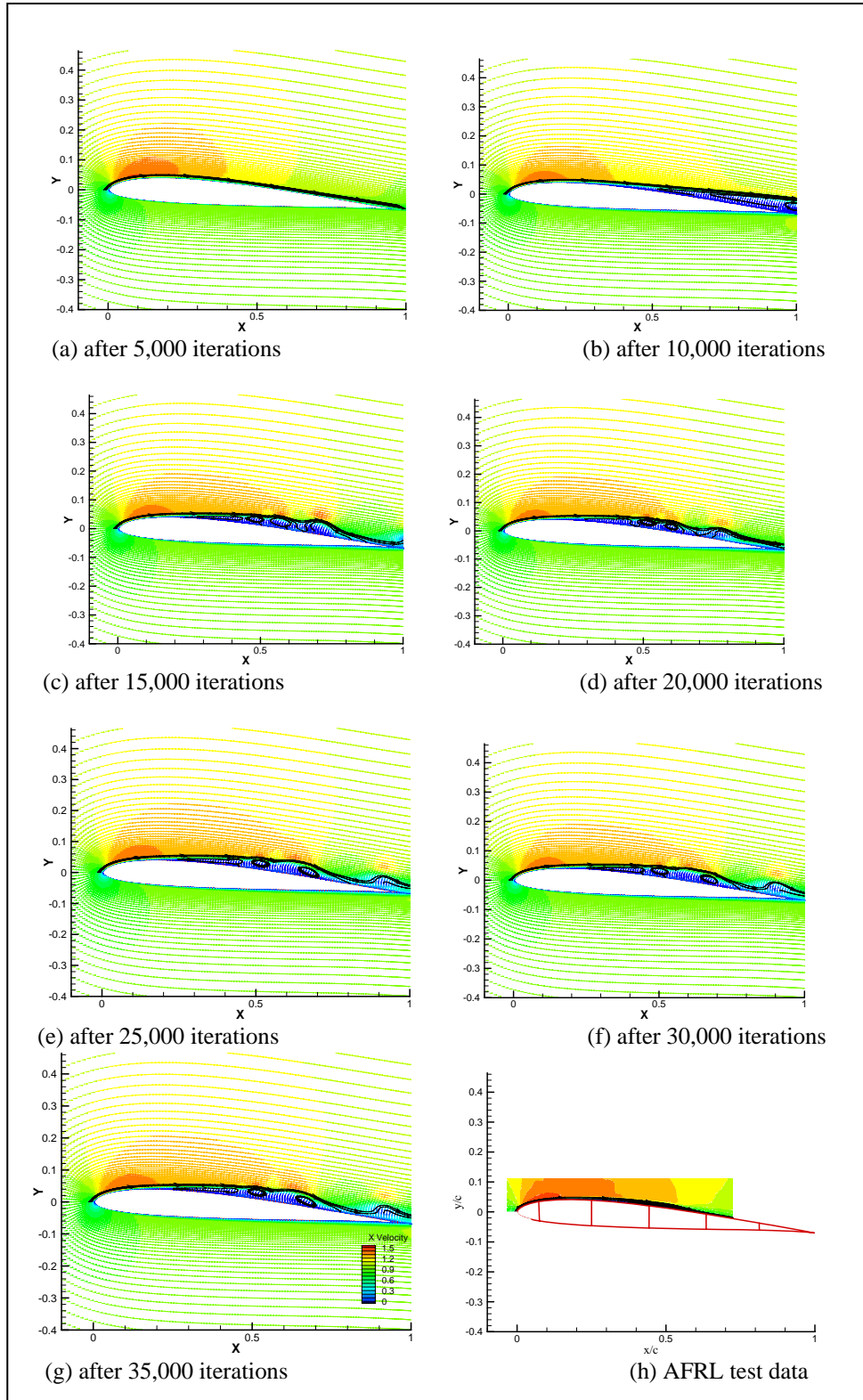


Figure 8 – Velocity Field and Streamlines

Besides insufficient iterations, another possible reason for people to miss capturing a stable laminar separation bubble in computation is the insufficient grid resolution. For a typical viscous computation like the current one, a mesh with 91 points in the normal direction and the first grid spacing of 10^{-5} of the chord length from the surface is usually sufficient to resolve the boundary layer flows. However, as shown in Figure 9, the surface C_p distribution predicted on this coarser mesh is very unstable, the same as Pauley et al.'s finding in [28]. Apparently although the resolution of this grid is sufficient to resolve the boundary layer, it is still not sufficient to resolve the laminar flow separation.

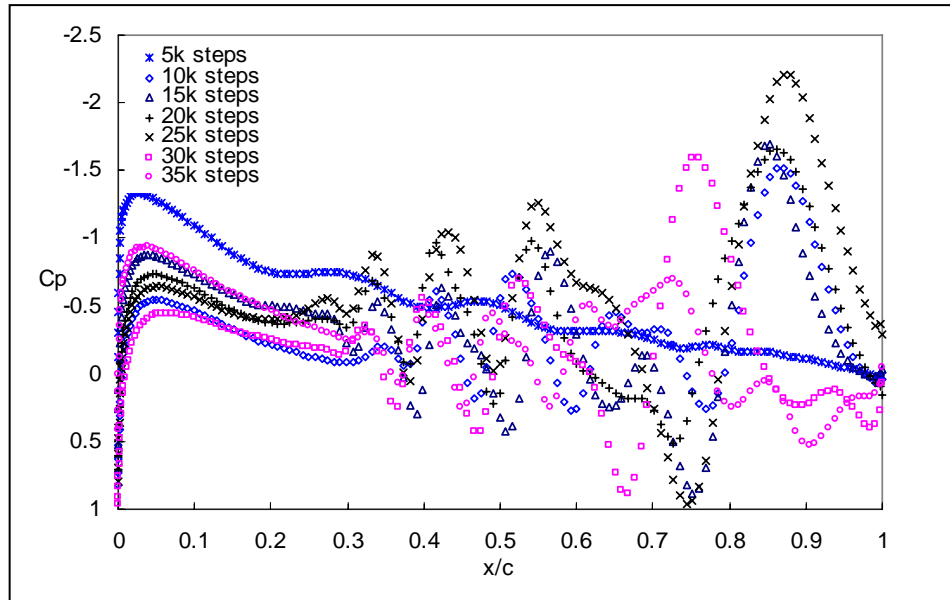


Figure 9 – Predicted Surface C_p Distribution on a Coarser Mesh with 91 Points in Normal Direction

4.2 Specification of Transition Point

A key for prediction of laminar separation bubble is how to specify the separation induced transition point. The existing transition prediction methods range from simple empirical correlations through semi-empirical methods like e^N method to direct numerical simulations. The e^N method, based on linear stability analysis and the empirical input of N at transition, is the most popular in practice. In [16], Stock and Haase investigated the feasibility of coupling e^N method to RANS computation. It is found that in order to produce reliable laminar data for the stability analysis, a sufficiently large and constant number of grid points are required inside the viscous layer. This requirement, combined with the stability analysis, render the resulting RANS computation much more intensive. In the following, we will present a much simpler method to locate the transition point.

Let us blow up Figure 8(g) near the upper surface of the airfoil. As shown in Figure 10, the flow next to the surface reverses the direction around $0.18c$, indicating the separation of laminar flow. From the separation point, a dividing line forms. Above this line, the flow moves downstream and below this line, the flow moves upstream, resulting in a strong free shear layer there. This

shear layer starts to become unstable from $0.4c$ and eventually rolls up into a vortex. At the same time, the reversed flow next to the upper surface reverses the direction again and moves downstream whereas in reality this should happen until the reattachment. Both phenomena are not physical and can be used as the indications of the fact that a laminar solution is unsustainable from there and the transition to turbulence should take place.

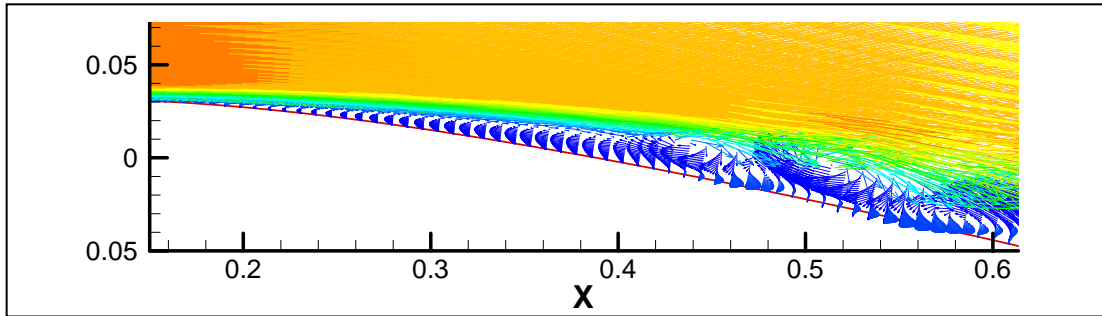


Figure 10 – Velocity Fields Adjacent to the Upper Surface of SD7003 Airfoil

To quantify the location of the transition point, the distribution of the tangential Mach numbers at the grid points next to the upper surface of SD7003 airfoil is further presented in Figure 11. It is found that the laminar solution is very smooth before the second flow reverse but becomes quite unstable after the second flow reverse. This further proves that the transition to turbulence should take place where the laminar solution next to the upper surface reverses the direction for the second time. According to Figure 11, the transition point for this low-Re SD7003 airfoil case is at $0.416c$ whereas the laminar separation point is at $0.176c$.

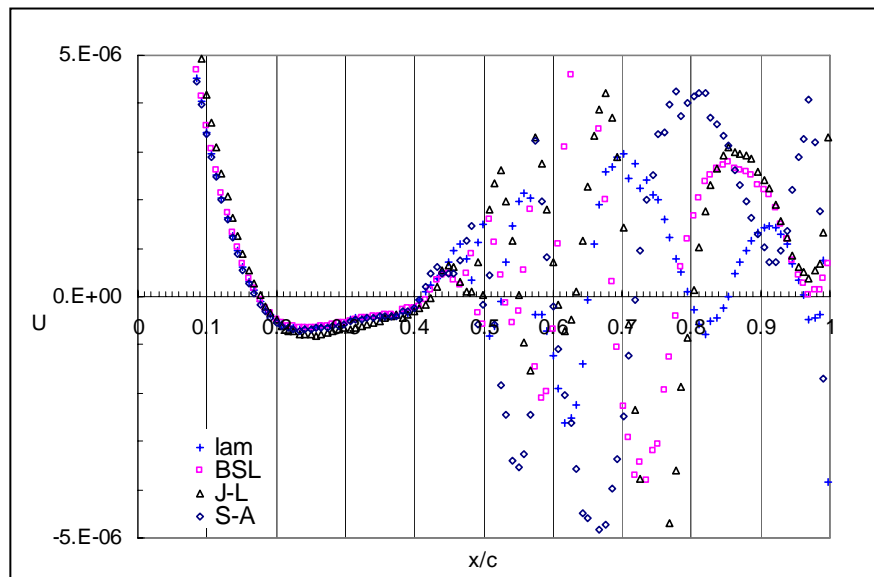


Figure 11 – Distribution of Tangential Mach Numbers next to the Upper Surface of SD7003 Airfoil

Also included in Figure 11 are the “laminar” solutions from RANS simulations with zero production terms in the selected turbulence models. The use of such RANS solutions as the

“laminar” solutions has two advantages. First, this will introduce less perturbation to the subsequent RANS computations in which the production terms in the turbulence models are turned on after the transition point. Second but more importantly, the effect of the freestream turbulence level on the transition point can be taken into account through the boundary conditions. It is found that the two solutions given by the laminar computation and the RANS simulation with Spalart-Allmaras (S-A) one-equation model [27] are almost indistinguishable up to the transition point. On the other hand, the solution given by the RANS simulation with Jones-Launder’s (J-L) $k-\varepsilon$ model [26] deviates from the laminar solution the most. The transition point given by the RANS simulation with Menter’s 2-layer BSL model [25] is one grid point later than the laminar solution and the S-A solution whereas J-L model delays the predicted transition position by another grid point from the BSL solution. All these findings are further supported by the surface C_p distributions shown in Figure 12. Among all RANS solutions, the S-A solutions are the closest to the laminar solutions in Figure 6. On the other hand, the initial discrepancy between the RANS solutions given by the two-equation models and the laminar solutions is quite large. However, the differences between the solutions up to the transition point become smaller with iterations. From the transition point, moreover, the solutions given by RANS with the two-equation models are found less stable than the laminar solutions.

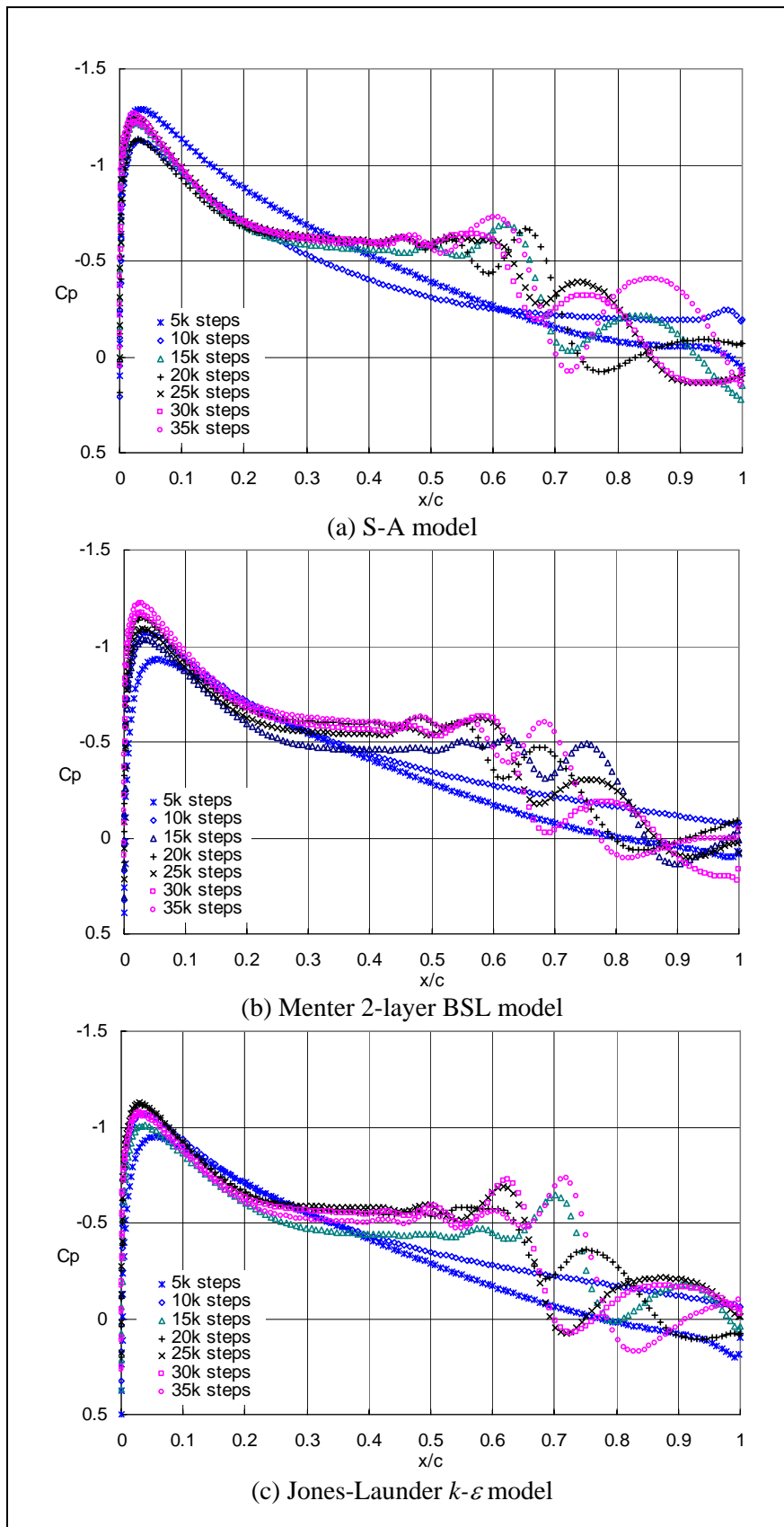


Figure 12 – Surface C_p Distributions Predicted by RANS with Zero Production Terms

4.3 RANS Solution of Low-Re SD7003 Airfoil Case

After locating the transition point, RANS simulations are performed with zero production terms in the selected turbulence model before the transition point and nonzero production terms after the transition point. To compare the convergence performance with the above laminar computation, we start RANS computation from the uniform freestream conditions again rather than restart the computation from the above RANS solutions with zero production terms in the selected turbulence model. It is found in Figure 13 that initially the numerical residual of RANS simulation with S-A model is almost the same as the laminar solution. However, different from the laminar solution, the numerical residual of RANS simulation does not jump back after 9,000 iterations. Instead the numerical residual drops monotonically. This is due to turn-on of the production term in the selected S-A model from the transition point.

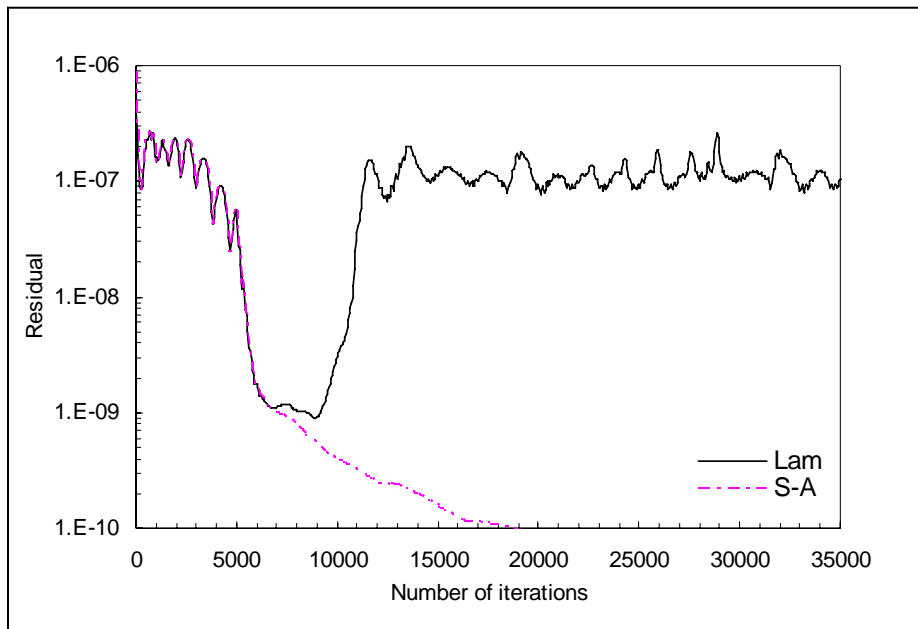


Figure 13 – Convergence History

The predicted surface C_p distributions over the upper surface of the airfoil by RANS simulations with different turbulence models are presented in Figure 14 along with the 3D LES result in [17]. It is found that the converged S-A solution is almost indistinguishable from the 3D LES result. On the other hand, the solutions given by the two-equation models are quite different from the 3D LES result. It is interesting to note that different from Horton's bubble model, the S-A solution does not immediately accelerate the deceleration process after the transition point. Instead the predicted flow keeps the same deceleration rate for a while and starts to decelerate quickly until after $0.532c$. On the other hand, consistent with Horton's model, the converged BSL solution speeds up the deceleration immediately after the transition point. The predicted deceleration rate is also larger than the 3D LES result, indicating the possibility of overpredicting Reynolds stress there. Furthermore, the converged J-L solution is found between the above two RANS solutions. The deceleration after the transition point speeds up before the S-A solution but after the BSL solution. The predicted deceleration rate is smaller than those given by the other

approaches, indicating the possibility of underpredicting Reynolds stress there. Also included in Figure 14 is the result given by RANS simulation with Abid's low-Re version of $k-\varepsilon$ model (Abid) [13] without specification of the transition point. It is found that this low-Re version of $k-\varepsilon$ model does capture the laminar separation bubble automatically but is unable to completely remove those humps found in the above laminar C_p distribution associated with the artificial vortical structures inside the boundary layer. Therefore, the flow reattaches the surface much later than the 3D LES result and the separation bubble is unreasonably long and thick.

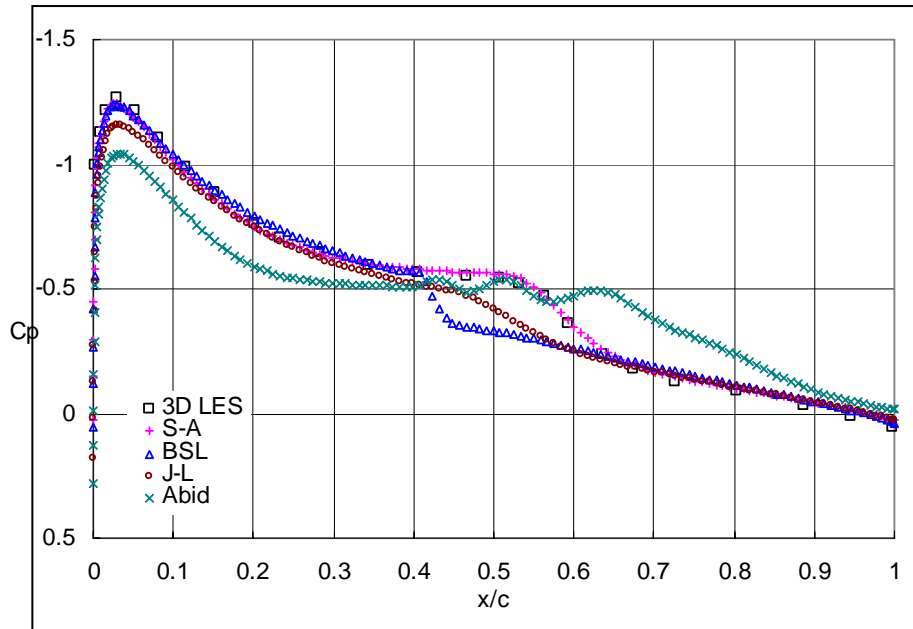


Figure 14 – Surface C_p Distributions Predicted by RANS with Transition

Figure 15 presents the predicted Reynolds stress distributions by RANS with the three turbulence models in comparison with AFRL test data in [21]. It is surprising to see that all RANS computations, especially Menter's 2-layer BSL model, underpredict the maximum absolute value of Reynolds stress. This is inconsistent with the predicted surface C_p distributions shown in Figure 14. A possible reason for that is we compare our RANS results with AFRL water tunnel test data instead of TU-BS wind tunnel test data. According to [17], the maximum absolute value of Reynolds stress in AFRL water tunnel test data is slightly larger than TU-BS wind tunnel test data. On the other hand, the starting position and shape of the predicted Reynolds stress pocket by S-A and J-L models agree with the test data well whereas the Reynolds stress pocket given by BSL model starts too early. Especially the predicted Reynolds stress by BSL model jumps to its maximum absolute value too quickly after the transition point. This is why the BSL surface C_p solution has a turning point immediately after the transition. Consistent with the surface C_p distributions shown in Figure 14, BSL model produces the largest maximum absolute value of Reynolds stress among all RANS solutions whereas J-L model gives the smallest one.

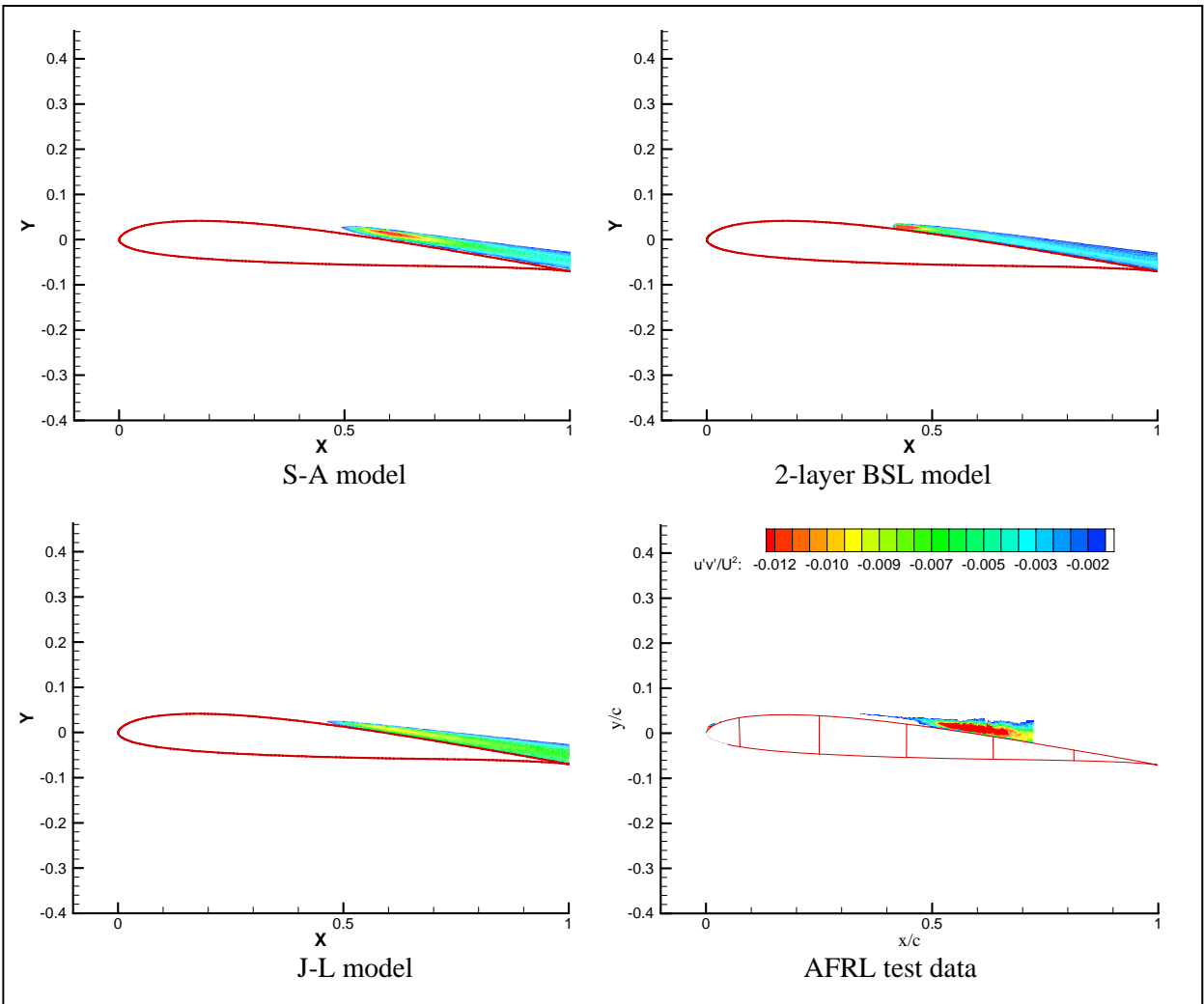


Figure 15 – Reynolds-stress Distributions

To further compare the predicted laminar separation bubble with AFRL test data, Figure 16 presents the velocity contours and streamlines around SD7003 airfoil. It is found that the separation bubble predicted by S-A model is the closest to the test data, including both the length and thickness, whereas those given by the two-equation models are too short and too thin. Especially the one from BSL model is almost negligible.

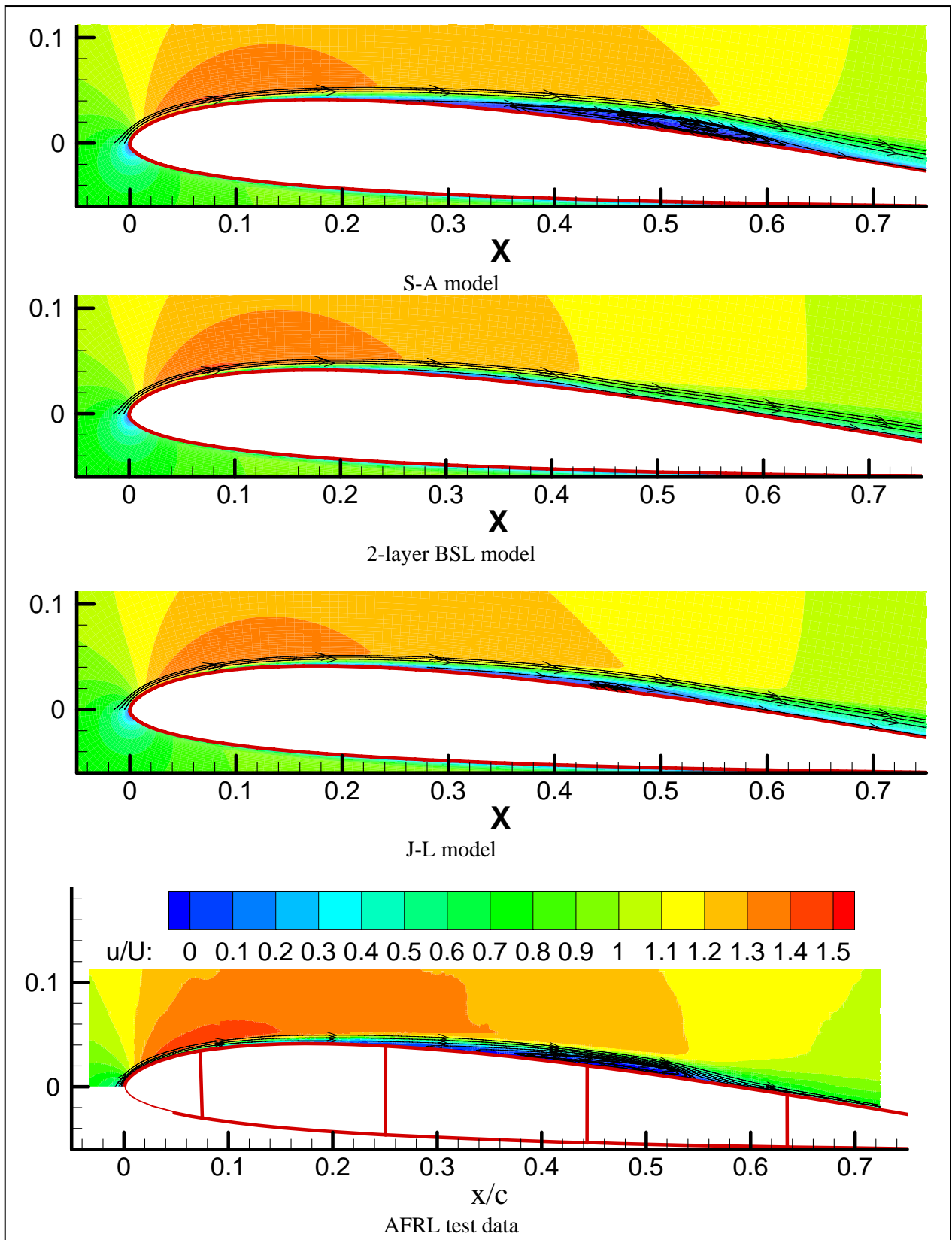


Figure 16 – Velocity Contours and Streamlines

These facts can be more clearly seen in the distributions of tangential Mach numbers next to the upper surface of airfoil shown in Figure 17. It is found that after turning on the production terms in the selected turbulence model after the transition point, the laminar separation point can be modified to a significantly later position. Especially for the BSL solution, there are only two grid points in the reversed flow state due to overprediction of Reynolds stress.

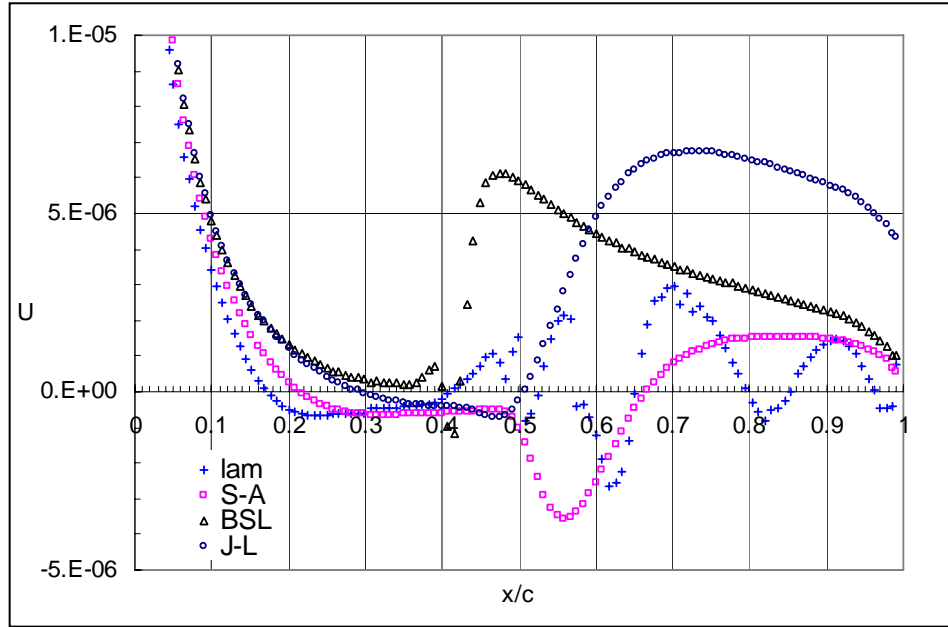


Figure 17 – Distribution of Tangential Mach Numbers next to the Upper Surface of SD7003 Airfoil

Table 1 further presents a quantitative comparison between the numerical separation bubble and the existing test data in [21]. Compared with the test data and 3D LES result, S-A model is found to predict a longer bubble whereas the two-equation models give a shorter bubble. Again the separation bubble predicted by 2-layer BSL model is almost negligible.

Table 1 – Comparison of Numerical and Experimental Results

	x_s/c	x_t/c	x_r/c
Test (TUBS)	0.30	0.55	0.62
Test (AFRL)	0.18	0.47	0.58
3D LES	0.25	0.49	0.60
S-A	0.22	0.42	0.67
BSL	0.40	0.42	0.42
J-L	0.30	0.43	0.51

4.4 *Application to Other Low-Re Airfoil Cases*

To examine the robustness of the developed method for prediction of low-Re airfoil aerodynamics, we will further investigate several other low-Re airfoil cases. This time RANS computations with zero production term in the selected S-A model are performed first to provide the baseline “laminar” solution. After determination of the transition point using the method developed above, RANS computations with the complete S-A model after the transition point are

restarted from the above RANS “laminar” solutions instead of the uniform freestream conditions for less numerical iterations before a fully converged RANS solution is achieved.

Eppler387 Airfoil

The first low-Re airfoil case investigated is the Eppler387 airfoil case in [3]. It is noteworthy that this test model has a blunted trailing edge with the thickness of 0.167 percent of the chord length. Our numerical results indicate that whether or not modeling this blunt trailing edge has a big impact on the predicted C_p suction peak value, especially for higher angle of attack. Figure 18 presents the two types of meshes we have used in computation. The first one is a C-mesh without modeling the blunt trailing edge. There are 301 points in the wraparound direction with 201 points on the body, and 151 points in the normal direction with the first grid spacing from the surface as 10^{-6} of the chord length. The second one is an O-mesh with modeling the blunt trailing edge. There are 251 points in the wraparound direction with 11 points to cover the blunt trailing edge, and 111 points in the normal direction with the first grid spacing from the surface as 10^{-6} of the chord length.

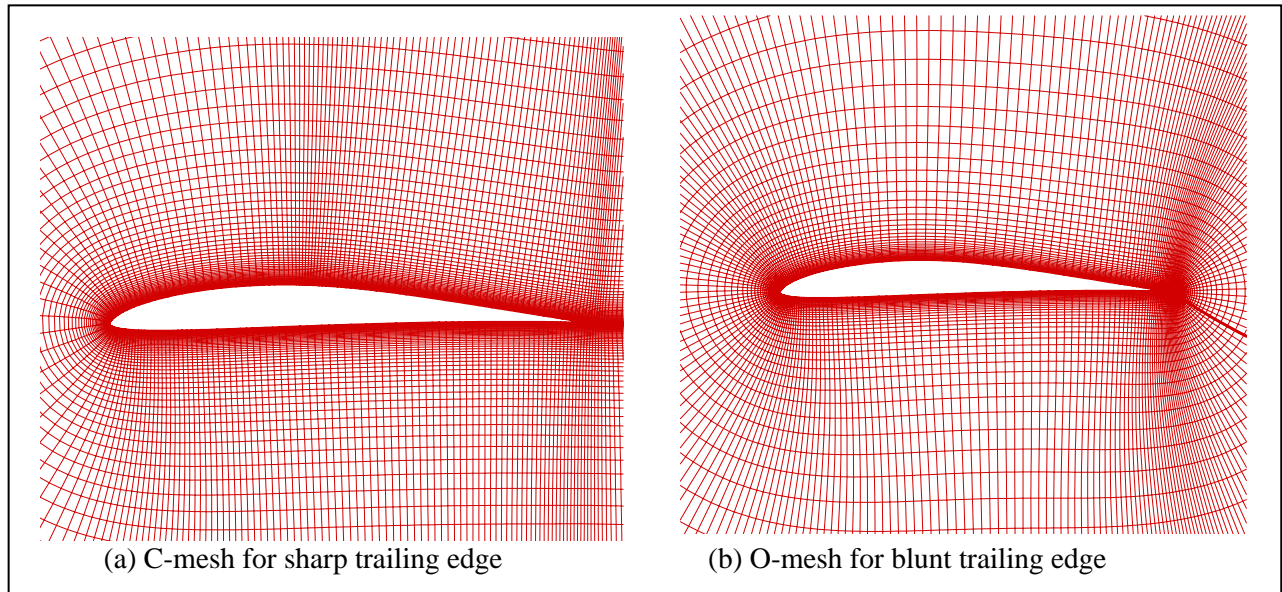


Figure 18 – Computational Grids Used for Eppler387 Airfoil Cases

There are many test conditions in [3]. The first one investigated here is the case with the freestream Mach number of 0.08, and the Re of 100,000, and the angle of attack of 7° . Figure 19 presents the predicted surface C_p distribution on the two computational grids in comparison with the test data from [3]. It is found that without modeling the blunt trailing edge, the predicted peak value of the surface C_p suction on the C-mesh is much lower than the test data. On the other hand, with modeling the blunt trailing edge, the predicted surface C_p distribution on the O-mesh is nearly the same as the test data.

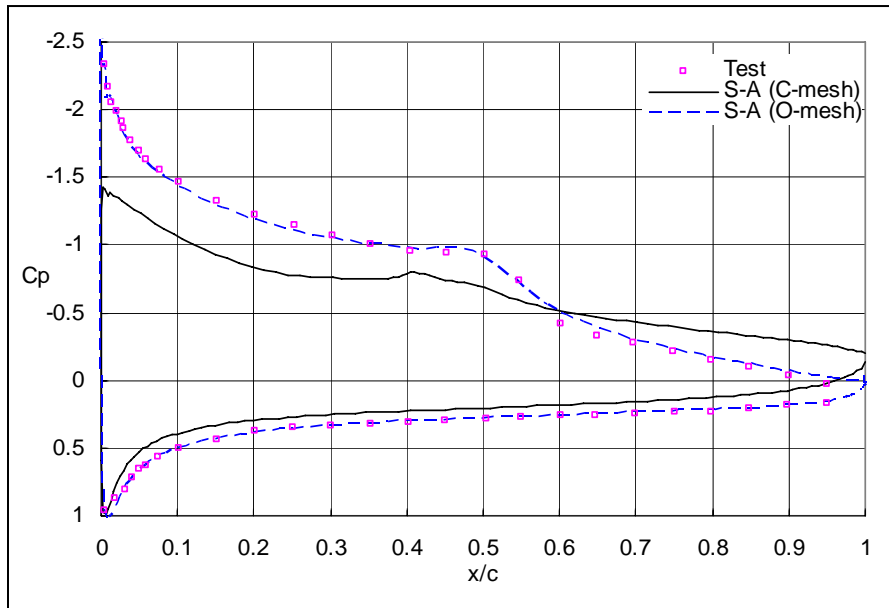


Figure 19–Surface Cp Distributions for Eppler387 Airfoil Case

Next, we will further investigate the most difficult cases in [3] with the Re of 60,000. At this Re , the flow is found not stable in the tests, making an accurate prediction very difficult. In Figure 20, we present the laminar solutions of C_L versus α on both C-mesh and O-mesh and the RANS solution using the S-A model and transition mechanism on C-mesh in comparison with the test data in [3]. As expected, the predicted C_L values on C-mesh with sharp trailing edge are smaller than those predicted on O-mesh with blunted trailing edge. This is because as shown in Figure 19, the former underpredicts the C_p suction peak value.

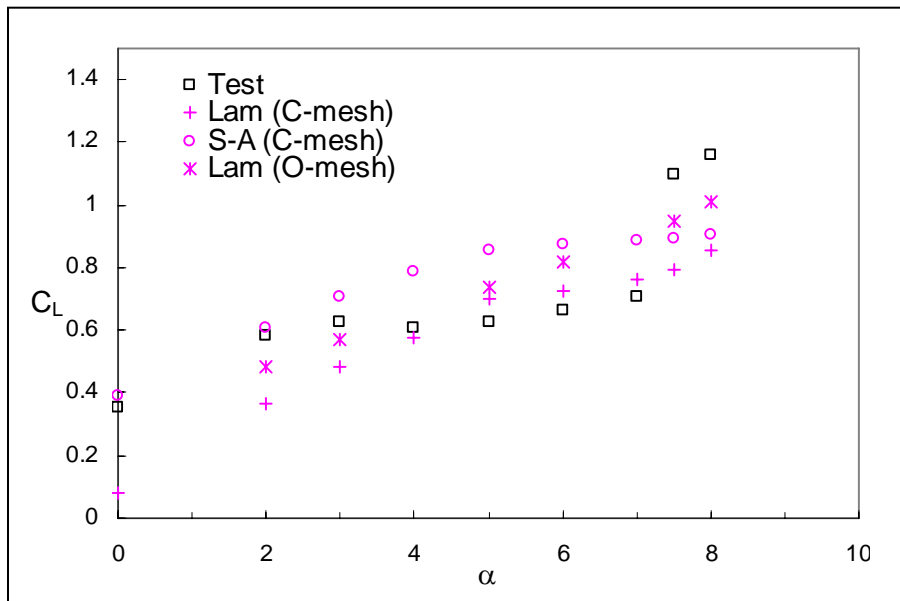


Figure 20–Lift Curve for Eppler387 Airfoil Case

LA203A Airfoil

The second investigated case is the low-Re LA203A airfoil case in [29]. Again an O-type mesh is used for this case. As shown in Figure 21, there are 161 points in the wraparound direction and 121 points in the normal direction with the first grid spacing from the surface as 10^{-6} of the chord length.

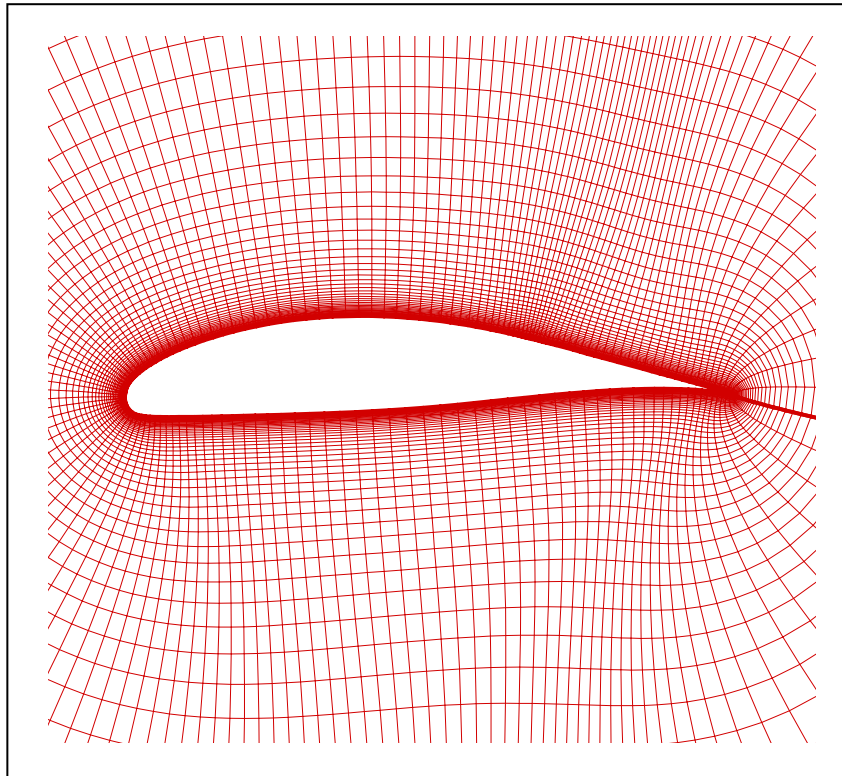


Figure 21–Computational Grid Used for LA203A Airfoil Case

The case investigated has the freestream Mach number of 0.1, and the Re of 250,000. The angle of attack is 4° . Figure 22 presents the predicted laminar and turbulent solutions of the surface Cp distribution. It is found that the obtained baseline laminar solution is already very close to the test data except that the Cp plateau is shorter compared with the test data. After turning on the production term in the S-A model after the transition point, the obtained solution is further improved.

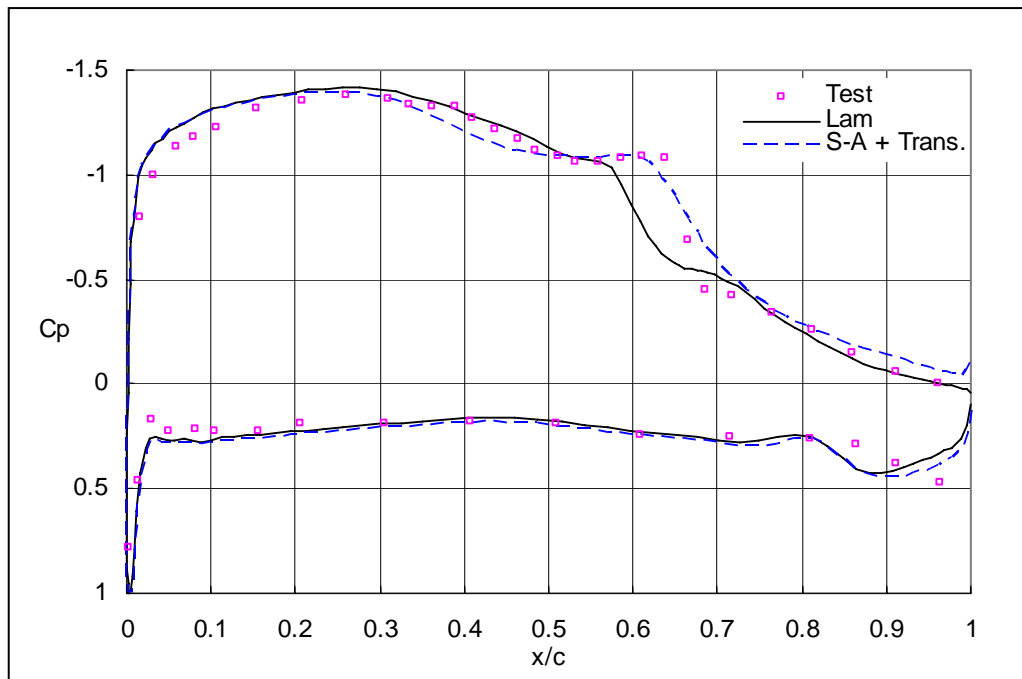


Figure 22–Surface Cp Distributions for La203a Airfoil Case

LNV109A Airfoil

The third case considered is the low-Re LNV109A airfoil case in [29]. A C-type mesh is used for this case. As shown in Figure 23, there are 281 points in the wraparound direction with 181 points on the body and 121 points in the normal direction with the first grid spacing from the surface as 10^{-6} of the chord length. The outer boundary of the grid is extended to 20 chords in all directions.

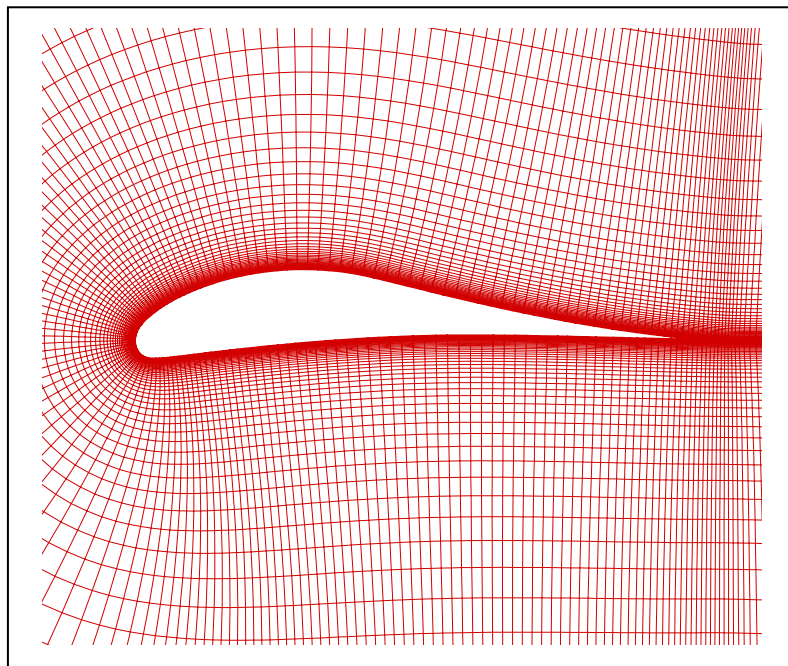


Figure 23–Computational Grid Used for LNV109A Airfoil Case

Figure 24 presents the predicted laminar and turbulent solutions of the surface C_p distribution in comparison with the test data in [29] for the case with the freestream Mach number of 0.1, and the Re of 375,000, and the angle of attack of 4° . It is found that after turning on the production term in the S-A model after the transition point, those numerical humps in the laminar solution of the surface C_p distribution after the transition point are removed. Otherwise the laminar and RANS solutions are very similar. Both have shorter C_p plateau than the test data. The importance of the baseline laminar solution on the accuracy of the final solution is clearly seen.

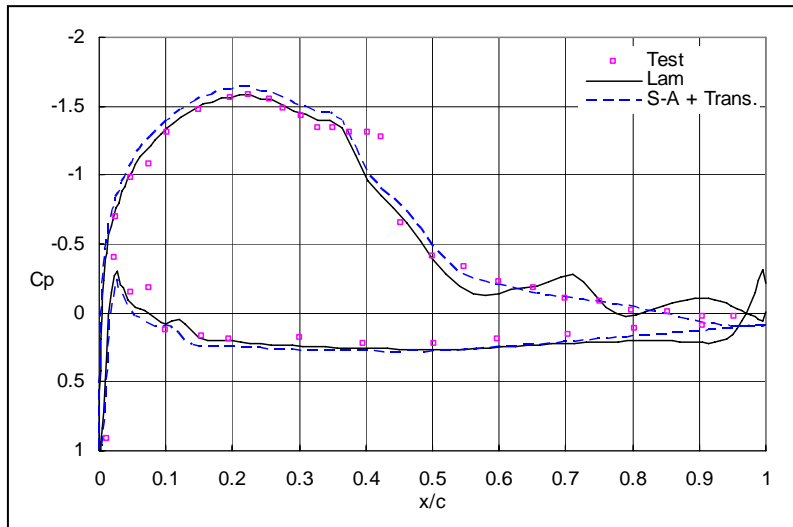


Figure 24–Surface C_p Distributions for LNV109A Airfoil Case

FX63-137 Airfoil

The next case considered is the low- Re FX63-137 airfoil case in [30]. A C-type mesh is used for this case. As shown in Figure 25, there are 291 points in the wraparound direction with 191 points on the body and 121 points in the normal direction with the first grid spacing from the surface as 10^{-6} of the chord length. The outer boundary of the grid is extended to 20 chords in all directions.

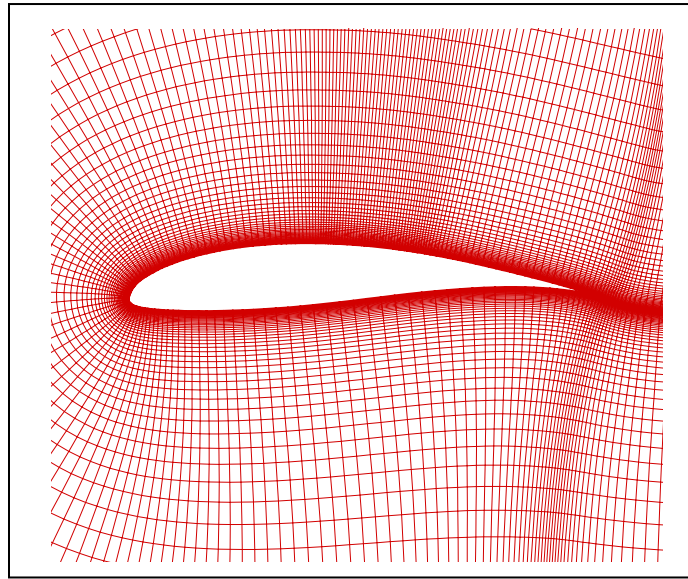


Figure 25–Computational Grid Used for FX63-137 Airfoil Case

Figure 26 presents the predicted laminar and turbulent solutions of the surface C_p distribution in comparison with the test data in [30] for the case with the freestream Mach number of 0.022, and the Re of 100,000, and the angle of attack of 7° . It is found that there are some numerical oscillations after the suction peak in the final surface C_p distribution, which also exist in the laminar solution. Apparently this problem is related to either the smoothness of the surface geometry definition we have got or the robustness of the applied low Mach number preconditioning method but has nothing to do with the developed transition mechanism in this Phase I work. After turning on the production term in the S-A model after the transition point, the obtained numerical solution is improved but still slightly different from the test data in [30]. A possible reason for this is that we have not digitized the test data accurately.

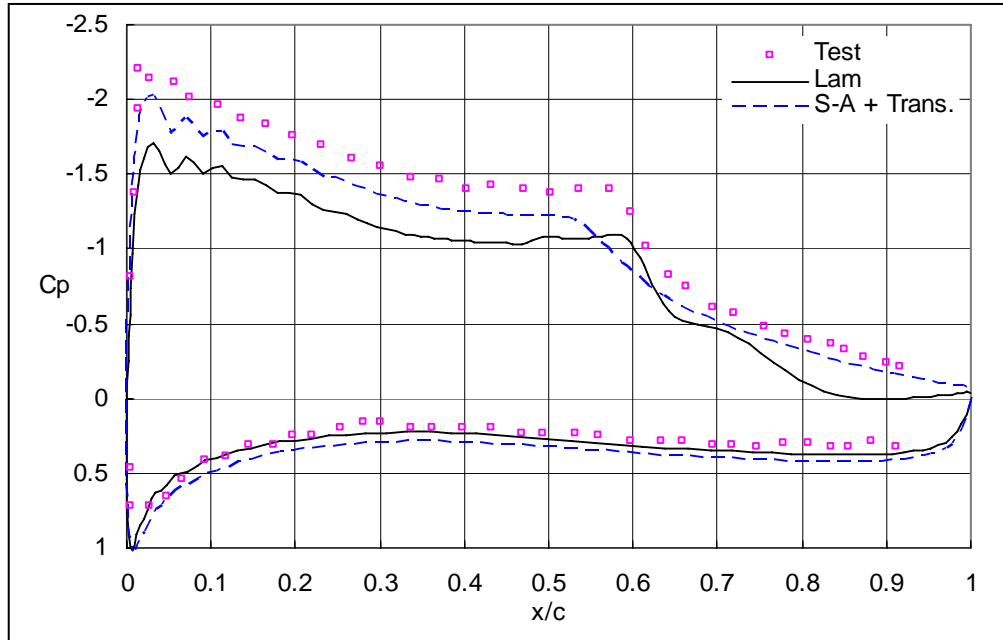


Figure 26–Surface C_p Distributions for FX63-137 Airfoil Case

5.0 QUASI-3D RANS SIMULATION OF LOW-RE SD7003 AIRFOIL CASE

Next, we will investigate the above low-Re SD7003 airfoil case again using a 3-D grid with 3 planes in the spanwise direction and using a periodic boundary condition along the spanwise direction. Each C-mesh plane is the same as the 2-D mesh used before with 386 points along the wraparound direction, and 280 points on the airfoil surface, and 151 points in the normal direction with the first grid spacing from the surface as 10^{-6} of the chord length. The grid spacing in the spanwise direction is 0.4 chords. Our objective is to investigate the effect of vortex stretching on the laminar separation bubble.

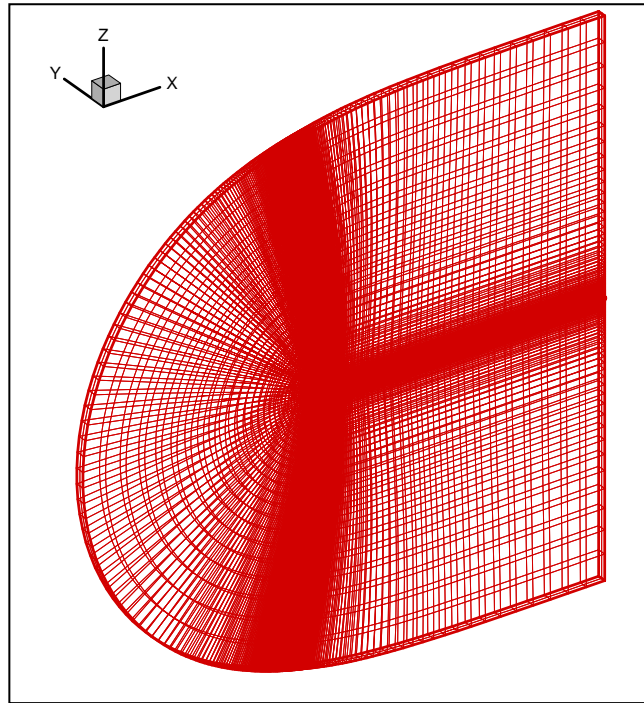


Figure 27 – Computational Grid

A laminar computation is performed first. The predicted surface C_p distribution over the upper surface of the airfoil at each spanwise station after 35,000 iterations is presented in Figure 28 together with the 2-D RANS solution and 3-D LES result. It is found that there is no visible difference between the obtained surface C_p distributions at each spanwise station, indicating no 3-D effect captured in the RANS computation. On the other hand, we do see that the quasi-3D solution is different from the 2-D solution, especially those artificial humps in the predicted surface C_p distributions. As mentioned in the last section, the artificial humps in the surface C_p distributions result from the artificial vortical structures. The difference between the quasi-3D solution and the 2-D solution indicates that the predicted vortical structures in the quasi-3D computation are different from those in the 2-D computation due to vortex stretching effect.

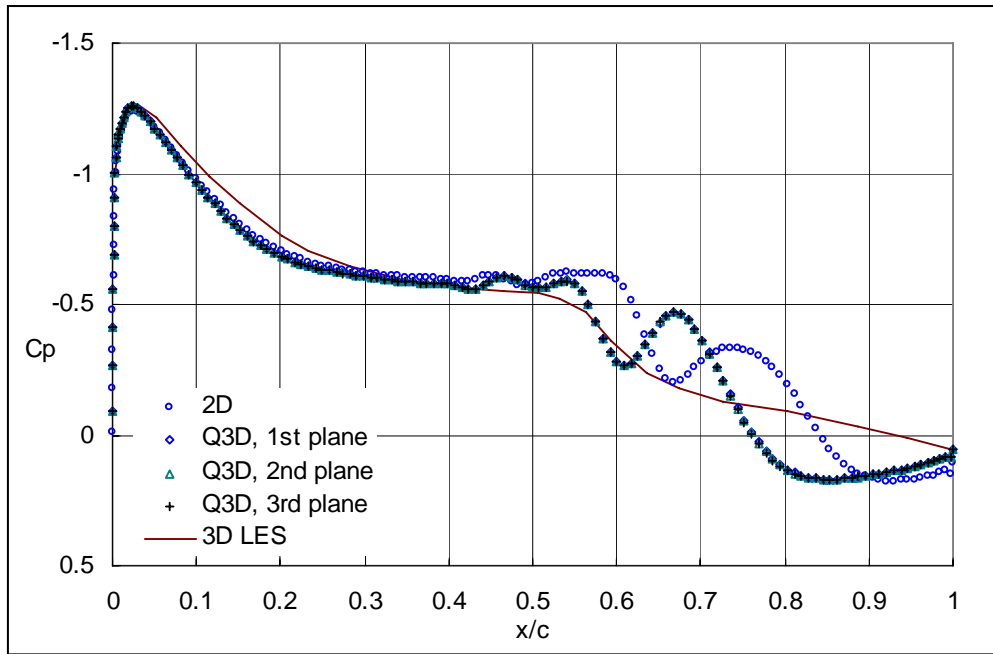


Figure 28 – Laminar Surface C_p Distributions on the Upper Surface of SD7003 Airfoil

Next, RANS computation is performed with the numerical method developed in the last section using the S-A turbulence model. The resulting surface C_p distributions over the upper surface of the airfoil are presented in Figure 29 together with the 2-D RANS result and 3-D LES result. This time we find that the quasi-3D solution is almost the same as the 2-D solution even though the 3-D transition location, $0.407c$, is slightly earlier than the 2-D transition location, $0.416c$.

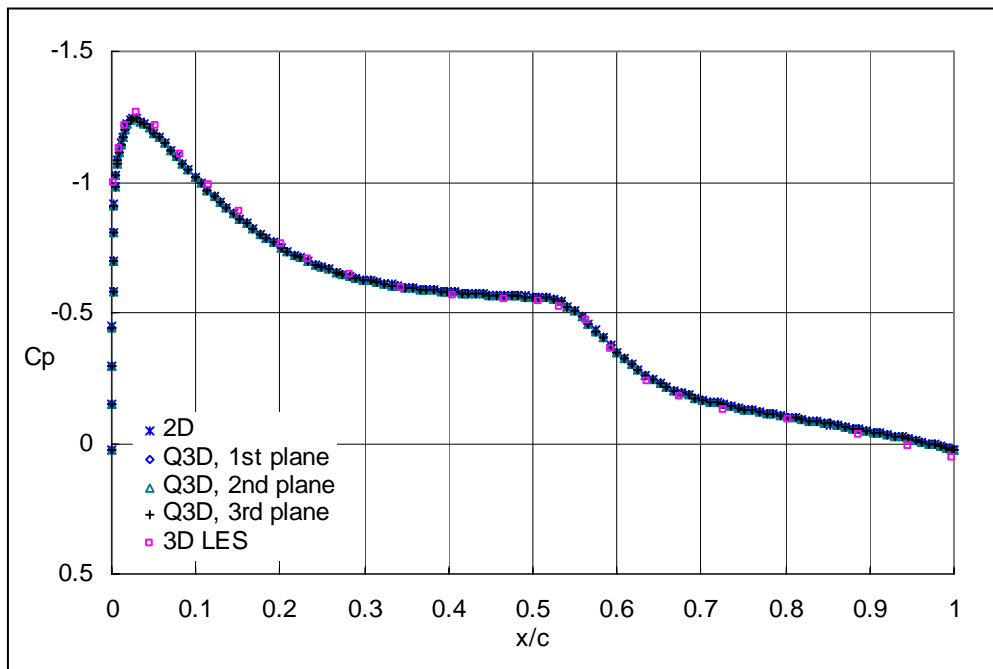


Figure 29 – S-A RANS Surface C_p Distributions on the Upper Surface of SD7003 Airfoil

6.0 RANS SIMULATION OF UNIVERSITY OF FLORIDA 5 IN. MAV WING

The real MAV wing configuration we select for investigation in Phase I is University of Florida (UF) 5in. MAV wing, as shown in Figure 30. This membrane wing has the root chord length of 4.09 in. and the wing span of 5 in. The wing area is 17.11 in². In Phase I, we only consider the rigid wing case.



Figure 30–UF MAV: Flexible Latex Rubber Wing

The computational grid around this wing configuration is provided by Prof. Wei Shyy. The grid was created using ANSYS ICEM CFD grid generation software based on the wing geometry exported from ProE. The multiblock structured grid has 18 blocks and 210,000 grid points. The wing surface is covered by 41 by 21 points. The top and bottom outer boundaries are at 6c distance from the wing whereas the outflow boundary is at 11c distance from the wing. Due to flow symmetry, only half of the wing is modeled.

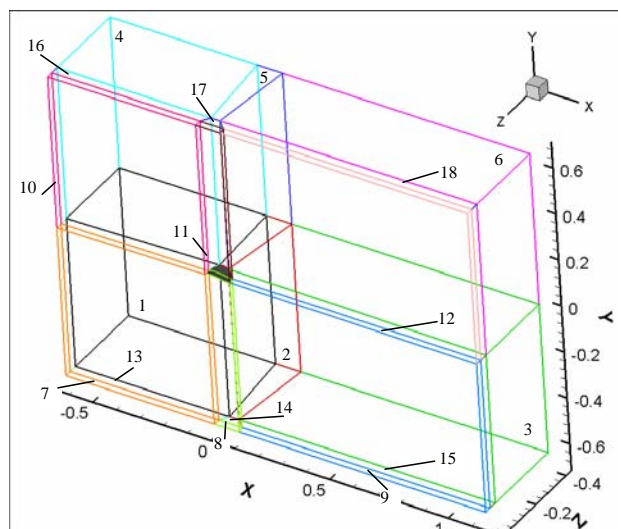


Figure 31–Computational Grid Blocks Layout

Based on our experience for SD7003 airfoil case, the resolution of the above grid is not sufficient for accurate simulation of laminar flow separation. So, we have refined the grids in the normal direction by reducing the first grid spacing from the surface to 10^{-6} of root chord length and increasing the number of grid points in the normal direction from 25 to 99 for each block.

Again a laminar computation is performed first. The flow conditions are: $M_\infty = 0.0294$ and $Re = 90,000$ based on the root chord length. To construct CFD solution database for POD analysis, a series of computations are performed at the selected training points: $\alpha = -5^\circ, 0^\circ, 5^\circ, \dots, 50^\circ$. The predicted laminar solution of surface density contours and entropy contours in 5 cutting planes are presented in the left-hand side of Figure 32. Also presented in the right-hand side of Figure 32 are the RANS solutions using the S-A turbulence model and the above developed transition mechanism. It is found that the surface density contours predicted by the two approaches are quite different, especially for higher angles of attack, where the turbulent flow regions are larger. On the other hand, the predicted tip vortex structures by the two approaches are quite similar. This is because we assume that outboard of the wing tips, the flow is always laminar.

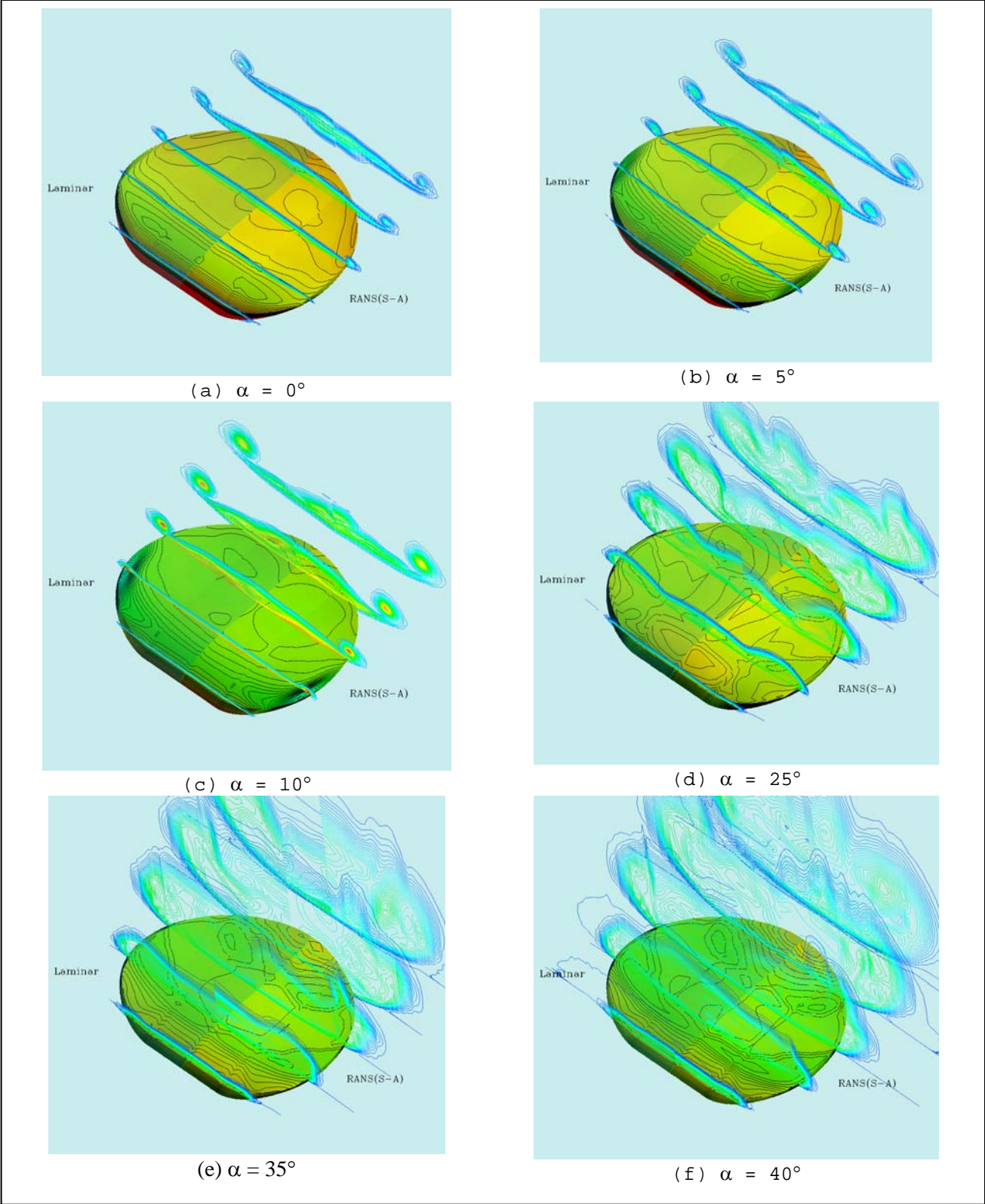


Figure 32–Flow Patterns around University of Florida 5 in. MAV Wing

7.0 POD RECONSTRUCTION OF MAV WING SOLUTION

A Navier-Stokes simulation is far too computationally expensive to be used for MAV stability and control analysis. Therefore, ZONA Technology proposes to use POD to further distill the computed data from Navier-Stokes simulations into reduced order models that can serve as the basis for further MAV stability and control analysis.

POD is a technique for extraction of a set of basis functions of the spatial variables that have maximum energy content, and thereby the capture of the principal structures, allowing for construction of a model of reduced dimension to approximate the original ensemble.

Let us assume the solution to be a series of steady state variations of the angle of attack whereby the angle of attack is treated just like time in conventional POD approaches for time dependent fluid flows. Therefore, for a given Mach number and Re,

$$f(\mathbf{x}, \alpha) = \sum_{k=1}^K \phi_k(\alpha) \psi_k(\mathbf{x}) \quad (8)$$

where $f(\mathbf{x}, \alpha)$ is the flow variable, $\phi_k(\alpha)$ is the scalar coefficient with α being the axis on which the flow field evolves, and $\psi_k(\mathbf{x})$ is the basis function. The same concept holds for angle of attack, Mach number, and Re as the axis to trace the variations in MAV flow fields.

The choice of $\psi_k(\mathbf{x})$ in Eq. (8) is not unique. To facilitate reduced-order modeling, POD searches for the optimal orthogonal basis functions $\bar{\psi}_k(\mathbf{x})$ in the sense that the linear combination of the first few basis functions gives an optimal convergence path for the series in Eq. (8), thus justifying its truncation well before all the K combinations. According to [31], this can be achieved by a singular value decomposition of the solution matrix S with each column representing a set of CFD solutions for each angle of attack. As a result, the above POD problem becomes a search for K eigenvectors corresponding to the K largest eigenvalues of the matrix SS^T . The Air Force's SNAPMAN2 software [32] is used to perform the POD analysis.

After obtaining those optimal basis functions, the flow variable in (8) can be represented by

$$f(\mathbf{x}, \alpha) = \sum_{k=1}^K \bar{\phi}_k(\alpha) \bar{\psi}_k(\mathbf{x}) \quad (9)$$

The rapid convergence of the norm of $E_{\bar{K}}(\mathbf{x}, \alpha) = f(\mathbf{x}, \alpha) - f^{\bar{K}}(\mathbf{x}, \alpha)$ with \bar{K} allows for a reduced-order modeling, where

$$f^{\bar{K}}(\mathbf{x}, \alpha) = \sum_{k=1}^{\bar{K}} \bar{\phi}_k(\alpha) \bar{\psi}_k(\mathbf{x}) \quad (10)$$

and $\bar{K} \ll K$. The percentage of the flow energy captured by a reduced-order model can be defined as

$$E_{\bar{K}} = \sum_{k=1}^{\bar{K}} \lambda_k / \sum_{k=1}^K \lambda_k \quad (11)$$

where λ_k is the eigenvalue of the matrix SS^T .

Results and Discussion

In this section, the results from our POD analysis of the high-level CFD solution database for University of Florida 5 in. MAV wing are presented. It is found that for higher angles of attack, an accurate POD reconstruction requires more modes.

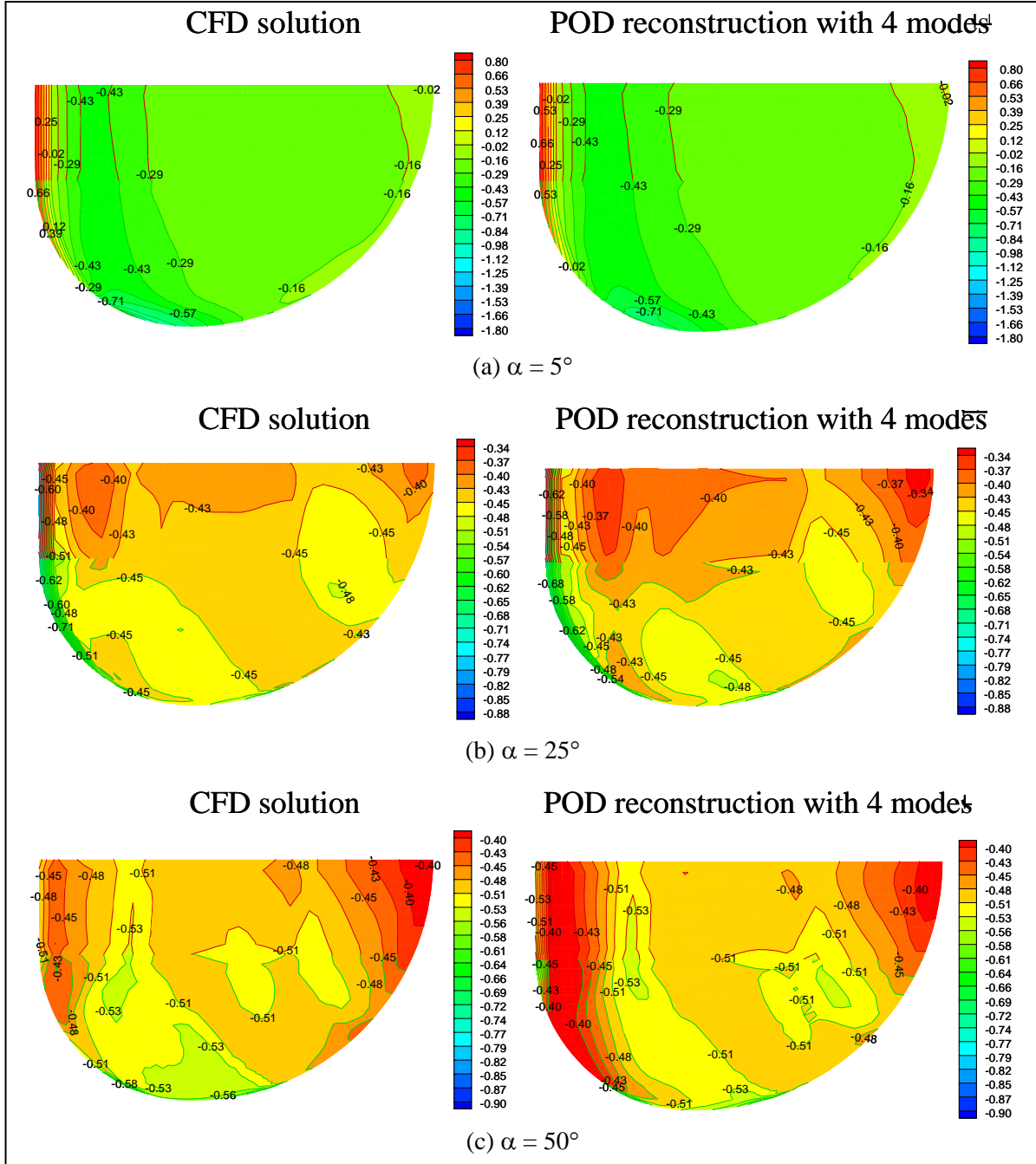


Figure 33–POD Reconstructions of Surface Cp Distribution

8.0 PHASE II PLAN

8.1 Phase II Objectives

The overall objective is to establish an enhanced aerodynamic methodology to handle a low-Re and/or a gusty flight regime encountered by a membrane-wing MAV for its control and performance. The specific technical objectives on Phase II include:

- a. *Establish an expedient computational method in low-Re aerodynamics for the performance and control of a membrane MAV (mMAV) wing in a gusty and a gust-free environment. The methodology should be able to predict airload/response due to gust on a rigid/flexible mMAV wing with occurring separation bubble and flow transition.*
- b. *Experimental verifications of the computational-aerodynamic solutions of an airfoil and a rigid mMAV wing in a gusty and/or a gust-free environment.*
- c. *Using the enhanced aerodynamic method developed to obtain time-domain forces and moments for the rigid/flexible mMAV thus providing inputs for a 3DOF/Simulink demonstration of the mMAV control/performance.*

8.2 Phase II Tasks

Six major tasks will be performed in Phase II which include.

(1) Rigid mMAV wing aerodynamics, (2) Flexible mMAV wing aeroelasticity, (3) Gust Considerations, (4) Perform Proper Orthogonal Decomposition/Response Surface Methodology (POD/RSM) of the Unsteady Flow for given flight parameters, (5) Water/Wind Tunnel Testings for solution validation, and (6) Perform 3DOF Simulink with POD/RSM data for MAV Stability/Control demonstration.

In order to perform such an aerodynamic development and control demonstration for a mMAV, we select the FLRW designed by the University of Florida and shown in Figure 30 as a testbed. The FLRW has a reflex chamber and has a size of 6 inches with a weight of 52 grams. It carries a color video camera and is powered by a Maxon electric motor to achieve speeds of 12 to 30 mph. Control is accomplished using two independently controlled elevons that are actuated symmetrically and anti-symmetrically using small rotary servos. In addition, because of the flexible structure that provides a passive adaptive washout mechanism, the FLRW can change in wing camber and wing twist in gusty wind conditions. This is to reduce the sensitivity of the FLRW to disturbance. Because of the flexible structure and the reflex camber which could increase the complexity of the flow structures, the FLRW is a challenging MAV design for accurate aerodynamic prediction. The success of the tasks proposed will certainly demonstrate that the enhanced-aerodynamic methodology is a powerful aerodynamic tool for the selected FLRW with a view that it can achieve the Phase II technical objectives of section 8.1 for a more general class of MAV.

8.2.1 Rigid mMAV wing aerodynamics

- Generalize the 2D work developed in Phase I to 3D flow for a rigid mMAV wing.
- The method will use RANS/CFL3D, and we will adopt the same transition flow model technique as that created for the 2D work.
- The obtained CFD solutions in terms of transition point locations, transition lengths, surface pressures, effects of vortex stretching and flow Reynolds stresses will be verified with experimental results in 8.2.4.

8.2.2 Flexible mMAV wing aeroelasticity

This is a grand task on a brand new look on the aeroelasticity of mMAV wing. The basic aeroelastic procedure of a tightly coupled aerodynamic CFD and structural interaction for the mMAV wing has been thoroughly worked out previously by Shyy et al [33]. However, the procedure is based on a Navier-Stokes/laminar flow model without the consideration of flow transition. Our proposed tasks are to reconstruct Shyy's procedure using the proposed unsteady RANS, or URANS/CFL3D, and to further generalize the rigid aerodynamics including the transition flow technique developed in 8.2.1 to that for a flexible mMAV.

- Reconstruct Shyy's procedure but using URANS/CFL3D instead
 - Moving grid technique
 - Membrane structural solver
- Implement the transition flow model technique of 8.2.1
- Select computed cases for comparison (e.g., in terms of rigid to elastic ratio)
 - Shyy's result vs present result (all aeroelastic)
 - Present rigid solution versus present aeroelastic

8.2.3 Gust Consideration

Adding the gust model into the rigid and flexible mMAV wing is an essential step for the present 3D development.

- Validate the formulated computational Gust approach/solutions with that of the classical aeroelasticity, i.e., Sharp-edge gust (Kussner function) and Traveling delta function gust (Sears function), etc.
- Generalize the 2D gust handling procedure for a 3D rigid mMAV wing (of 8.2.1). Evaluate the effect on flow transition and separation due to gust.
- Extend the gust handling procedure of 8.2.1 to a flex mMAV wing (of 8.2.2). Evaluate the flow transition and flow separation effects due to gust.
- Select computed cases for comparison (e.g., in terms of rigid to elastic ratio).

8.2.4 Wind/Water - Tunnel Testing

Professor Luis Bernal of the ZONA team will use the water-tunnel and the wind-tunnel facilities at University of Michigan for testing the rigid/flexible mMAVs. Anticipated steps include

- Test model fabrication: Rigid model, flexible model.
- Equipments/DPIV procedure set up.

- Investigation on flow about a pitching 3D rigid MAV wing. Measure unsteady effects on rigid-wing airload/response.
- Investigation on flow about Flexible membrane MAV wing.
- Measured data is to be validated by ZONA with ZONA computed solutions, e.g., in terms of forces and moments.

8.2.5 Perform POD/RSM of the Unsteady Flow of 3.2 for Given Flight Parameters

The POD/RSM development here is to provide interpolated solutions for stability and aerodynamic performance evaluation in an expedient manner.

- POD/RSM of a rigid mMAV wing (of 8.2.1) for baseline stability/flight dynamic analysis.
- POD/RSM of a flexible mMAV wing (of 8.2.2) for stability/control and assure aerodynamic performance.
- POD/RSM should treat the gust modeling as an individual parametric vector.

8.2.6 MAV Flight Simulation Model

The simulation model will be based on the six degree-of-freedom nonlinear body-fixed equations of motion that result from the MAV longitudinal and lateral/directional decoupled dynamics,

$$\begin{aligned}
\dot{u} &= \frac{F_x}{m} - qw + rv - g \sin \theta \\
\dot{v} &= \frac{F_y}{m} - ru + pw + g \cos \theta \sin \varphi \\
\dot{w} &= \frac{F_z}{m} - pv + qu + g \cos \theta \cos \varphi \\
\dot{p} &= \frac{1}{I_x} \left[L + \dot{r}I_{xz} - qr(I_z - I_y) + pqI_{xz} \right] \\
\dot{q} &= \frac{1}{I_y} \left[M - pr(I_x - I_z) + r^2I_{xz} - p^2I_{xz} \right] \\
\dot{r} &= \frac{1}{I_z} \left[N - pq(I_y - I_x) + \dot{p}I_{xz} - qrI_{xz} \right]
\end{aligned} \tag{12}$$

where $u(t)$, $v(t)$, $w(t)$, $p(t)$, $q(t)$ and $r(t)$ are the perturbed forward, lateral and vertical speeds, as well as the roll, pitch and yaw rates of the MAV, respectively. There is coupling between the longitudinal and lateral/directional dynamics due to the inertial and gravitational terms.

The MAV physical constants to be considered are the mass, m , the wing area, S , the wing span, b , the mean aerodynamic chord \bar{c} , and the matrix of inertia about the rigid-body axis, I^b , that is

$$I^b = \begin{bmatrix} I_x & -I_{xy} & -I_{xz} \\ -I_{xy} & I_y & -I_{yz} \\ -I_{xz} & -I_{yz} & I_z \end{bmatrix} \tag{13}$$

The aerodynamic forces, and pitching moment are produced by the MAV relative motion with respect to the air flow, and are proportional to the dynamic pressure $q_\infty = 0.5\rho_{air}V^2$ as well as to the angle of attack, $\alpha(t)$, and sideslip angle, $\beta(t)$, with respect to the relative wind. In addition to the two aerodynamic angles and dynamic pressure, they are dependent on the Re.

Then, the aerodynamic forces (F_x , F_y and F_z) and moments (L , M and N), that appears in the above equation will be computed as the end product of the CFD simulation runs by the POD/RSM approach. Their nonlinear functional dependence on the aerodynamic angles, dynamic pressure and Re will be modeled along this Phase II effort throughout the use of “look-up” tables in the Matlab/Simulink software environment.

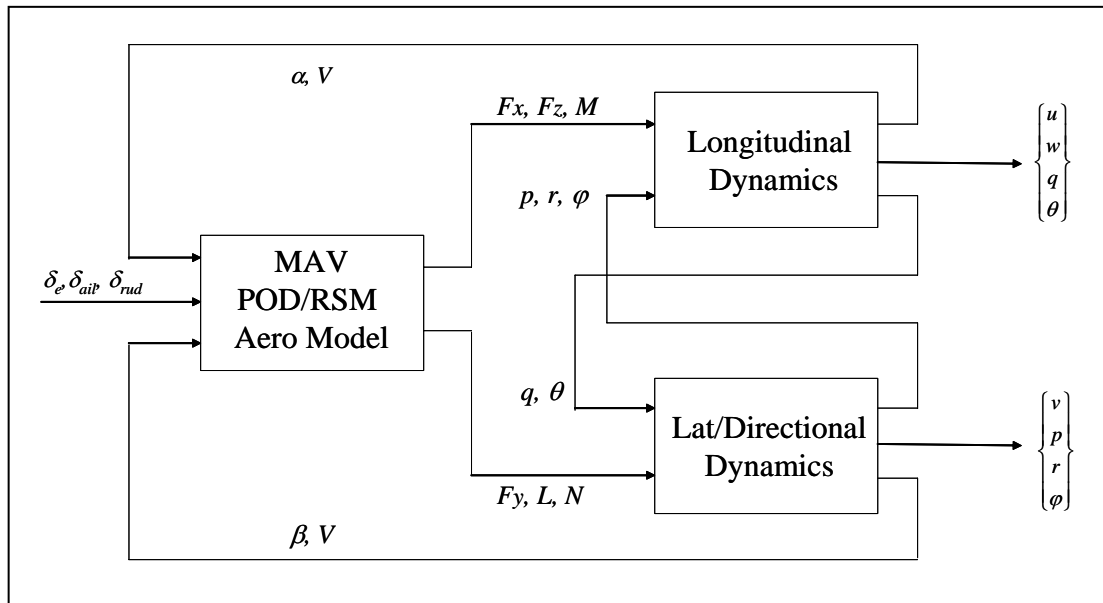


Figure 34 MAV 6-DOF Implemented in the Simulink Environment.

The nonlinear equations of motion and the aerodynamic forces and moments computed using the proposed POD/RSM approach will be implemented in the MATLAB/Simulink environment system as shown in Figure 34.

It is clearly observed that, the inputs are the symmetrical, δ_e , and anti-symmetrical, δ_{ail} , elevon deflection angles, as well as the rudder deflection angle, δ_{rud} , while the outputs are the longitudinal and lateral/directional perturbed variables.

8.2.7 Planned Program Schedule

The planned program schedule for performing the proposed 6 tasks and showing the distribution of tasks between ZONA and University of Michigan is presented as follows:

Tasks	Year 1												Year 2												To Be Preformed By			
	1	2	3	4	5	6	7	8	9	10	11	12	1	2	3	4	5	6	7	8	9	10	11	12				
Task 1: Rigid MAV Wing Aerodynamics • Use RANS to investigate 2D/3D effects • Use RANS to obtain Forces/Moments • Validation w/ Test data	█																								ZONA/UM			
Task 2: Flexible mMAV Wing Aeroelasticity • Use URANS for Cp, Airload, Response on wing • Study Shyy's results vs RANS results • Evaluate Elastic/Rigid Ratio • Validation w/ Test data				█																						ZONA/UM		
Task 3: Gust Considerations • 2D Gust models revisit and CFD formulation • Use URANS for 2D gust effects on spt'n/transit'n • Use URANS for 3D gust effects on spt'n/transit'n														█														ZONA
Task 4: Wind/Water Tunnel Testing • Equipment/ PIV setup • Investigate the steady flow of a 3D rigid MAV wing • Investigate flow about a pitching 3D rigid MAV wing • Investigate flow about Flexible mMAV wing	█																								UM			
Task 5: Perform POD/RSM on Data of Tasks 1 / 2							█									█									ZONA			
Task 6: Perform 6DOF/Simulink for mMAV using Data from Task 5															█												ZONA	
Task 7: Final Report Documentation.																						█				ZONA/UM		
Program Management • Kick-off • Interim Report • Final Report/Final Presentation	▲			▲		▲		▲		▲				▲		▲		▲		▲		▲		▲				

Note: UM is the University of Michigan

9.0 REFERENCES

1. Volkers, D. F., "Preliminary Results of Windtunnel Measurements on Some Airfoil Sections at Reynolds Numbers between 0.6×10^5 and 5.0×10^5 ," Memo. M-276, Dept. of Aerospace Engineering, Delft Univ. of Technology, 1977.
2. Mueller, T. J. and Batill, S. M., "Experimental Studies of the Laminar Separation Bubble on a Two-Dimensional Airfoil at Low-Reynolds Numbers," AIAA-80-1440.
3. McGhee, R. J., Walker, B., and Millard, B., "Experimental Results for the Eppler 387 Airfoil at Low Reynolds Numbers in the Langley Low-Turbulence Pressure Tunnel," NASA TM 4062, 1988.
4. Selig, M., Donovan, J., and Fraser, D., *Airfoils at Low Speeds*, H. A. Stokely Publisher, 1989.
5. Mueller, T. J., "Aerodynamic Measurements at Low Reynolds Numbers for Fixed Wing Micro-Air Vehicles," RTP AVT/VKI Special Course on Development and Operation of UAVs for Military and Civil Applications, VKI, Belgium, 1999.
6. Young, L. A., Aiken, E. W., Derby, M. R., Demblewski, R., and Navarrete, J., "Experimental Investigation and Demonstration of Rotary-Wing Technologies for Flight in the Atmosphere of Mars," Proceedings of 58th Annual Forum of the AHS, Montreal, Canada, 2002.
7. Corfeld, K. J., "Computational Analysis of a Prototype Martian Rotorcraft Experiment," M.S. thesis, The Pennsylvania State University, 2002.
8. Shum, Y. K., and Marsden, D. J., "Separation Bubble Model for Low Reynolds Number Airfoil Applications," *Journal of Aircraft*, Vol. 31 (1994), pp.761-766.
9. Drela, M., and Giles, M. B., "Viscous-Inviscid Analysis of Transonic and Low Reynolds Number Airfoils," *AIAA Journal*, Vol. 25 (1987), pp.1347-1355.
10. Dini, P., Selig, M. S., and Maughmer, M. D., "Simplified Linear Stability Transition Prediction Method for Separated Boundary Layers," *AIAA Journal*, Vol. 30 (1992), pp.1953-1961.
11. Dini, P., and Maughmer, M. D., "Locally Interactive Laminar Separation Bubble Model," *Journal of Aircraft*, Vol. 31 (1994), pp.802-810.
12. Launder, B. E., and Sharma, B. I., "Application of the Energy-Dissipation Model of Turbulence to the Calculation of Flow near a Spinning Disc," *Letters in Heat and Mass Transfer*, Vol. 1 (1974), pp.131-138.
13. Abid, R., "Evaluation of Two-Equation Turbulence Models for Predicting Transitional Flows," *International Journal of Engineering Science*, Vol. 31 (1993), pp.831-840.
14. Wilcox, D. C., "Simulation of Transition with a Two-Equation Turbulence Model," *AIAA Journal*, Vol. 32 (1994), pp.247-255.
15. Liu, S. Z., and Tsai, H. M., "Simulation of Boundary Layer Transition with a Modified $k-\omega$ Model," AIAA-98-0340.
16. Stock, H. W., and Haase, W., "Feasibility Study of e^N Transition Prediction in Navier-Stokes Methods for Airfoils," *AIAA Journal*, Vol. 37 (1999), pp.1187-1196.
17. Yuan, W. X., Khalid, M., Windte, J., Scholz, U., and Radespiel, R., "An Investigation of Low-Re Flows past Airfoils," AIAA-2005-4607.
18. Spalart, P. R., and Strelets, M. Kh., "Mechanism of Transition and Heat Transfer in a Separation Bubble," *Journal of Fluid Mechanics*, Vol. 403 (2000), pp.329-349.

19. Van Ingen, J. L., "A Suggested Semi-Empirical Method for the Calculation of the Boundary Layer Transition Region," Delft Univ. of Technology, Dept. of Aerospace Engineering Rept. VTH-74, Delft, The Netherlands, 1956.
20. Smith, A. M. O., and Gamberoni, N., "Transition, Pressure Gradient, and Stability Theory," Douglas Aircraft, Rept. ES 26338, Long Beach, CA, 1956.
21. Ol, M. V., McAuliffe, B. R., Hanff, E. S., Scholz, U., and Kähler, C., "Comparison of Laminar Separation Bubble Measurements on a Low Reynolds Number Airfoil in Three Facilities," AIAA-2005-5149.
22. Krist, S.L., Biedron, R.T., and Rumsey, C.L., CFL3D User's Manual (Version 5.0), NASA Langley Research Center, April 24, 1998.
23. NASA CFL3D Version 6 Site. <http://cfl3d.larc.nasa.gov/Cfl3dv6/cfl3dv6.html>
24. Weiss, J. M., and Smith, W. A., "Preconditioning Applied to Variable and Constant Density Flows," *AIAA Journal*, Vol. 33 (1995), pp.2050-2057.
25. Menter, F. R., "Two-Equation Eddy-Viscosity Turbulence Models for Engineering Applications," *AIAA Journal*, Vol. 32 (1994), pp.1598-1605.
26. Jones, W. P., and Launder, B. E., "The Prediction of Laminarization with a Two-Equation Model of Turbulence," *International Journal of Heat and Mass Transfer*, Vol. 15 (1972), pp.301-314.
27. Spalart, P., and Allmaras, S., "A One-Equation Turbulence Model for Aerodynamic Flows," AIAA-92-0439.
28. Pauley, L. L., Moin, P., and Reynolds, W. C., "The Structure of Two-Dimensional Separation," *Journal of Fluid Mechanics*, Vol. 220 (1990), pp.397.
29. Liebeck, R. H., and Camacho, P. P., "Airfoil Design at Low Reynolds Number with Constrained Pitching Moment," Presented at the Conference on Low Reynolds Number Airfoil Aerodynamics, University of Notre Dame, Notre Dame, IN, UNDAS-CP-77B123, 1985.
30. Brendel, M., and Mueller, T. J., "Boundary Layer Measurements on an Airfoil at Low Reynolds Numbers," *Journal of Aircraft*, Vol. 25 (1988), pp.612-617.
31. Zhang, B., Lian, Y., Shyy, W., "Proper Orthogonal Decomposition for Three-Dimensional Membrane Wing Aerodynamics", AIAA-2003-3917.
32. Beran, P., "Snapman2 – Snapshot Manager V2.0", AFRL, 2004.
33. Shyy, W., Ifju, P., and Viieru, D., "Membrane Wing-Based Micro Air Vehicles," *Applied Mechanics Reviews*, Vol. 58, July 2005, pp. 283-301.

LIST OF ACRONYMS AND ABBREVIATIONS

ACRONYM	DESCRIPTION
AFRL	Air Force Research Laboratory
ANSYS ICEMCFD	Commercial CFD meshing program
BSL	Menter's Baseline shear layer model
CFD	Computational fluid dynamics
CFL3D	NASA CFD solver program
Cp	Pressure coefficient
DNS	Direct numerical simulation
FLRW	Flexible latex rubber wing
J-L	Jones-Launder
LES	Large eddy simulation
Low-Re	Low Reynolds number
MAV	Micro air vehicle
mMAV	Membrane MAV
POD	Proper orthogonal decomposition
R&D	Research and development
RANS	Reynolds-averaged Navier-Stokes
RSM	Response surface methodology
S-A	Spalart-Allmaras
TU-BS	Technische Universitat zu Braunschweig
UF	University of Florida
URANS	Unsteady RANS